A Study of the Nonlinear Acoustic Response of Area-contractions and Sense-lines

by

Thomas Wayne Teasley II

A thesis submitted to the Graduate Faculty of
Auburn University
in partial fulfillment of the
requirements for the Degree of
Master of Science

Auburn, Alabama
May 5, 2018

Keywords: Combustion, Instability, Acoustic Response, Impedance, Sense-line.

Copyright 2017 by Thomas Wayne Teasley II

Approved by

Dr. David E. Scarborough, Chair, Assistant Professor of Aerospace Engineering
Dr. Brian S. Thurow, Department Chair and Professor of Aerospace Engineering
Dr. Roy J. Hartfield, Walt and Virginia Woltosz Professor of Aerospace Engineering

Abstract

Rocket and gas turbine engine combustion instabilities, which lead to rapid engine failure through enhanced heat transfer rates and high-cycle fatigue, continue to be a serious concern for engineers. Experimental pressure measurements remain the best approach in determining the susceptibility of an engine to acoustically coupled combustion instabilities. However, the harsh, high-temperature environment requires that pressure transducers be remotely mounted to the engine's main chamber using “sense-lines”, creating an area-contraction at the connection point between the sense-line and combustor. Preliminary measurements have shown large discrepancies between sense-line measured and engine pressure amplitudes. To elucidate these discrepancies, this experimental study measured the nonlinear acoustic response of the area-contraction and sense-line with and without purge air flow. To do this, a multiple-microphone impedance tube was used to measure the acoustic impedance of the combined area-contraction and sense-line. Measurements were performed over a range of frequencies, area-contraction ratios, acoustic velocity amplitudes, and sense-line length-to-diameter ratios. These measurements revealed the acoustic response of the sense-line and area-contraction combination is highly nonlinear.

Acknowledgments

I would like to first extend my gratitude to Dr. Scarborough, Dr. Thurow, and Dr. Hartfield for their patience and commitment to my success in graduate school. Especially to Dr. Scarborough for his expertise in the complex field of acoustics. I also want to acknowledge Andy Weldon for taking the time to teach and demonstrate key principles in machining so that I may become a better engineer.

Having spent the better part of the last decade in college, I've learned that hard work and persistence is the key to anyone's success, especially my own. Overcoming walls and rising to challenges that I never thought I would have the ability to meet was a daily task for me. It isn't until now that I fully understand that the obstacles in my life have shaped my character.

I would never have been able to do this work without the support of my wife Molly, who encourages me to just "get a little more work done" every day. Her interest in nature and science drives my own to better understanding the intricacies of our physical world and universe. Finally, my parents Nancy and Wayne, have always supported me and encouraged my pursuit of science and engineering to which I am grateful.

Table of Contents

Chapter 1 Introduction 1

Chapter 2 Background and Theory 6

Chapter 3 Impedance Tube Best Practices and Literature Review 15

3.1 A Comparison of Impedance Tube Measurement and Driving Methods 15

3.2 Sensitivity Analyses and Error in Impedance Tube Measurement Methods 19

3.3 Significant Gaps in the Acoustic Response Data of Area-Contractions 22

Chapter 4 Experimental Facility 26

4.1 Data Acquisition and Control 31

4.2 Introducing of Steady Mean Flow into the Impedance Tube 33

Chapter 5 Data Reduction Procedures 35

5.1 Calibration Process 36

5.2 Complex Amplitude and Acoustic Velocity 39

5.3 Isolation of the Area-Contraction Calculation of impedance 39

5.4 DPT Confirmation Experiments and Sensitivity Study 40

5.5 Data Repeatability 46

Chapter 6 Results and discussion 48

6.1 A Study on Varying Area-Ratio Sense-Lines 48

6.1.1 Frequency Response of Different Area-Ratio Extension-Tubes 49
6.1.2 Sense-Line Impedance 53
6.1.3 Extension-Tube Impedance 55
6.1.4 The Acoustic End-Correction 57
6.1.5 Area-Contraction Impedance 60
6.1.6 Area-Contraction Describing Function and Experimental Data Collapsing 61
6.2 A Study on the Acoustic Response of Sense-Lines with Steady Mean Flow 64
6.2.1 Frequency Response of a Single Sense-Line with Flow 64
6.2.2 Sense-Line Impedance with Reverse Purge Air Flow 66
6.2.3 Extension-Tube Impedance with Reverse Purge Air Flow 68
6.2.4 Area-Contraction Impedance with Reverse Purge Air Flow 70
6.2.5 Sense-Line Impedance with Forward Purge Air Flow 72
6.2.6 Extension-Tube Impedance with Forward Purge Air Flow 74
6.2.7 Area-Contraction Impedance with Forward Purge Air Flow 76
Chapter 7 Conclusions 78
7.1 Future Work 80
Reference Pages 81

List of Tables

Table I. Average experimental data used in calculating the acoustic end-correction. 58

List of Illustrations and Figures

Figure 1: Illustration of the coupling between heat release and acoustic oscillations. 1

Figure 2: Plot of acoustic pressure and heat release oscillations versus time for an unstable, premixed combustion system. 2

Figure 3: Schematic of an acoustic sense-line configuration branching from an acoustic cavity attached to the injection plate of a fictional liquid rocket engine. 3

Figure 4: Area-contraction and sense-line combination where the area-contraction is located at x=0 and the sense-line is of length L with an area of S_2. 4

Figure 5: (a) Incompressible flow streamlines for an abrupt area-contraction with the flow direction going from region 1 to region 2. (b) Incompressible flow streamlines for an abrupt area-expansion with the flow direction from region 2 to region 1.[25] 9

Figure 6. Steady flow imposed on an acoustic velocity oscillation vs. time. 10

Figure 7: Sense-line attached to the fully functional impedance tube. 29

Figure 8. Schematic of the measurement head, simulated sense-line, acoustic sensors and hypothetical incident, reflected and transmitted acoustic waves. 30

Figure 9. LabView control interface for National Instruments c-DAQ. 31

Figure 10. Control diagram of the impedance tube data acquisition process..... 32

Figure 11. P&ID flow schematic for introduction of steady mean flow through orifice plate and sense-line/ impedance tube combination. 33

Figure 12. From left to right: orifice housing with internal step change, shim-stock laser-cut orifice, and speaker plug with perforated disc for free air flow..... 34

Figure 13. The reconstructed time domain signal (black) overlaid on the scaled original time domain signal (red). 36

Figure 14. Microphones threaded into an end plate of the impedance tube used for calibration. 37

Figure 15. A) Uncorrected pressure histories versus time for each DPT. B) Corrected pressure histories versus time for each DPT. 38

Figure 16: Measurement error compared to data taken with a short sensor spacing of 76.2 mm and 127 mm from a rigid end termination. 44

Figure 17: Measurement error compared to data taken with a long sensor spacing of 76.2 mm and 279.4 mm from a rigid end termination. 44

Figure 18. (a) Magnitude of the reflection coefficient and (b) phase of the reflection coefficient as a function of frequency for a closed – closed impedance tube for validation. 45

Figure 19: From top to bottom, (a) The magnitude of the reflection coefficient, (b) phase of the reflection coefficient, (c) acoustic power absorption coefficient, (d) and the magnitude of the acoustic velocity and acoustic pressure as a function of frequency for the (a) 5.08, (b) 10.44, (c) 16.89, and (d) 23.22 mm diameter sense-lines. 50

Figure 20. Magnitude and phase of the reflection coefficient for a 402.6 mm long extension-tube illustrating the acoustic response of an area-ratio equal to 1. 52

Figure 21: The measured acoustic resistance as a function of the acoustic velocity amplitude at the ¼ wave mode frequency for extension-tubes with area-ratios of 4.6, 8.6, 21.53, and 122.84. 54

Figure 22: The acoustic resistance as a function of the acoustic velocity amplitude at the ¼ wave resonance of each extension-tube in this study at the low-amplitude driving range. (a) view of all four area-ratio extension-tubes, (b) view of the lowest three area-ratios. 55

Figure 23. Resistance as a function of acoustic velocity amplitude as taken in each extension-tube. 56

Figure 24. Acoustic resistance as a function of the acoustic velocity amplitude for solely the effects of the area-contraction measured at the ¼ wave resonance of each extension-tube in question. 60

Figure 25. Low amplitude resistance versus acoustic velocity amplitude for the four area ratios in question isolating the effects of the sense-line. 61

Figure 26. Collapsed acoustic resistance of each area-contraction as a function of the acoustic velocity amplitude measured at the ¼ wave resonance of each extension-tube case with an average $K_L = 0.8173$. 63

Figure 27. Magnitude of the reflection coefficient and acoustic velocity amplitude versus frequency for a single sense-line length and diameter with varying steady mean flow rates..... 65

Figure 28. The acoustic resistance versus acoustic velocity amplitude measured at the ¼ wave mode frequency of 205 Hz for varying steady mean flow rates. 67

Figure 29. Resistance as a function of acoustic velocity amplitude measured in the extension-tube with varying steady mean flow rates..... 69

Figure 30. Acoustic resistance versus acoustic velocity amplitude with varying steady mean flow rates in the negative direction relative to the impedance tube with the effects of the area-contraction isolated. 71

Figure 31. Acoustic resistance versus acoustic velocity amplitude for flow rates applied in the positive direction of the impedance tube. 73

Figure 32. Resistance as a function of acoustic velocity amplitude measured in the extension-tube with varying steady mean flow rates in the forward direction. 75

Figure 33. Acoustic resistance versus acoustic velocity amplitude with varying steady mean flow rates in the positive direction relative to the impedance tube with the effects of the area-contraction isolated. 76

Nomenclature and Abbreviations

$\hat{A}_{corr}$ =Corrected complex pressure amplitude

$\hat{A}_{corr\,avg}$ = Corrected average complex pressure amplitude

$AF_{ref,i}$ = Amplitude scaling factor of the reference sensor to any other sensor

AMP_{fft} = Frequency-domain pressure amplitude

c =Speed of sound

$conj(t)$ = Complex conjugate function

D =Diameter of impedance tube based upon the cutoff frequency for higher order modes

DPT = Dynamic pressure transducer

d_{SL} =Diameter of the sense-line

$\delta\hat{P}_R$ =Induced error in the measurement of the complex pressure ratio

$\delta\phi_{ref,i}$ =Phase difference between the reference sensor phase and any other sensor phase

$\hat{E}_R$ =Complex total measurement error

$f_{anti-res}$ = Anti-resonance frequency

f_{res} =Resonance frequency

FFT =Fast Fourier transform

G =Rayleigh equation gain

G_{amp} =Amplifier electronic gain setting

k_i^+ = Wavenumber subjected to flow in the positive direction

k_i^- = Wavenumber subjected to flow in the negative direction

K_L =Geometric loss coefficient

L =Length of the subject under consideration i.e. impedance tube, sense-line

L_i =Position of any sensor other than the reference relative to the rigid termination

L_1 =Position of the reference sensor relative to the rigid termination

L_{eff} =Effective length of the sense-line

L_{geo} =Geometric length of the sense-line

L_{corr} =Length correction

ΔL =Incremental additional length of vibrating air outside of the sense-line

$M_{0,i}$ =Measured Mach number of the flow inside the impedance tube at sensor *i*.

n =Wave mode

$\bar{n}_{V_0}$ =Unit vector in the direction of steady mean flow velocity

$\bar{n}_x$ =Unit vector in the direction of the positive coordinate x-direction

N_s =Total number of samples

$\hat{p}_i$ =Complex pressure measured by sensor $i = 1, 2, 3$

$\hat{p}^*$ =Complex conjugate of the complex acoustic pressure

$P_{measured}$ = Measured pressure

$\hat{P}_R$ =Complex pressure ratio

$\phi_{ref,i}$ =Phase angle of the reference sensor or sensor $i = 2,3$

ϕ =Phase

ρ =Density of air

$\hat{R}$ =Complex reflection coefficient

S =Sensor sensitivity in millivolts per psi

$S_{IT,SL}$ =Cross sectional area of the impedance tube or sense-line

SPL =Sound pressure level

s =Sensor spacing

σ =Area ratio

t =Time or time index

TMB =Transducer mounting block

$\hat{u}$ =Complex acoustic velocity

V =Measured voltage

ω =Angular frequency

x_i =Negative position of sensor $i = 1,2,3$ relative to the rigid termination

Z_0 =Specific acoustic impedance equal to density multiplied by the speed of sound

$\hat{\zeta}$ =Dimensionless impedance of the area-contraction and the sense-line

$\hat{\zeta}_{ac}$ =Dimensionless impedance of the area-contraction, impedance tube, or sense-line

$\hat{Z}_{sp\,ac}$ =Acoustic impedance of the area-contraction and sense-line combination per unit area

Chapter 1

Introduction

The power generating gas turbine industry is approximately worth 20 billion USD globally.[1] In 2015, the net worth of the space industry, utilizing solid, liquid, and hybrid rocket engines for space propulsion, was estimated to be 330 billion USD globally.[2] These two industries hold considerable value in the world market, and when problems arise in testing or fielding these expensive engines, costly maintenance and downtime result in substantial loss in revenue. The reliability of solid and liquid rocket engines, used in missile defense systems, is also of serious concern for national security reasons. One of the leading causes for concern in both markets is thermo-acoustic oscillations, i.e., combustion instabilities.

Combustion instabilities are caused by a dynamic coupling between the heat release oscillations and acoustic pressure oscillations as shown in Figure 1. Example data of these high amplitude heat release and acoustic pressure oscillations in a laboratory combustor are shown in Figure 2. The resulting acoustic velocity oscillations cause increased heat and mass transfer rates leading to high-cycle fatigue and failure of structural engine components, leading to costly maintenance and downtime.

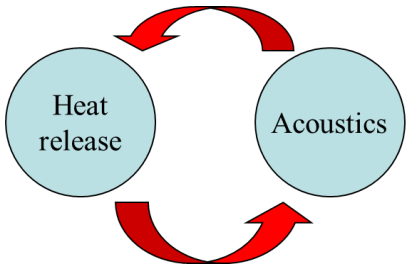

Figure 1: Illustration of the coupling between heat release and acoustic oscillations.

Combustion instabilities are particularly distressing in that the problem often arises unexpectedly. Historically, otherwise stable combustors can suddenly become unstable when operating conditions or ambient conditions change. Component wear as the engine system ages, not

to mention a seemingly minor modification of combustion system hardware, could also cause unexpected combustion instabilities or can result in an inoperable engine. Modifications as simple as moving fuel injection location, changing fuel injector hole size, or moving a perforated plate or swirl vane can cause a combustor to become unstable.[3]

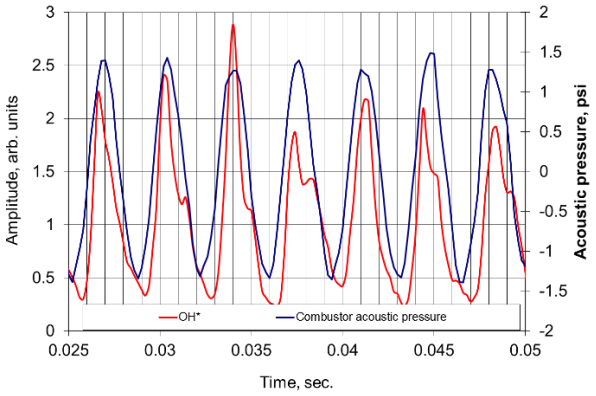

Figure 2: Plot of acoustic pressure and heat release oscillations versus time for an unstable, premixed combustion system.

It has been said that, at least to date, there is no single solution to the problem of combustion instabilities. Rather, most designers and manufacturers employ teams of engineers dedicated to adapting a complement of fixes to the problem. Due to the severity, importance, and large costs involved in the problem of combustion instabilities, a great deal of time, money, and effort has gone into developing several passive [4-21] and active [22] methods to prevent or eliminate these combustion instabilities and into testing combustion system hardware to determine stable operating conditions, testing combustion instability damping hardware, and generally trying to address combustor problems. These fixes have traditionally been applied to unstable combustion systems using the costly and time-consuming "cut-and-try" approach.

What is needed is a rational approach for testing and understanding these instabilities at realistic operating conditions for stable combustor operation and engineering level acoustic instability detection tools that allows designers to quickly and efficiently assess the acoustic stability characteristics of a given design at the early design stages and to investigate a wide range of options to mitigate combustion instabilities once a problem has been encountered. This

framework should be useful to a designer who are not themselves an acoustics expert. One possible framework is a measurement tool that allows the user to obtain high-accuracy high-resolution experimental acoustic response measurements of the natural acoustics of an engine. However, these measurements are difficult to obtain due to the corrosive and high-temperature environment of combustors. Sensors, such as dynamic pressure transducers, are not able to withstand this environment for extended periods of time, if at all. A work around that effectively removes the transducers from this harsh reacting environment is an acoustic sense-line.

A sense-line is a metal duct of some length and diameter with a transducer remotely mounted at one end. By employing the use of sense-lines for pressure measurements, an area-contraction is created at the connection point between the sense-line and the combustion chamber. This area-contraction has an associated impedance to acoustic forcing, which causes a modification of the acoustic pressures amplitude and phase that is communicated to the transducer at the other end of the sense-line. In fact, the acoustic impedance, which is defined as the ratio of the acoustic pressure to the acoustic particle velocity[23], behaves nonlinearly with frequency. Additionally, purge air flow of an inert gas is often introduced into sense-lines to further protect the sensors

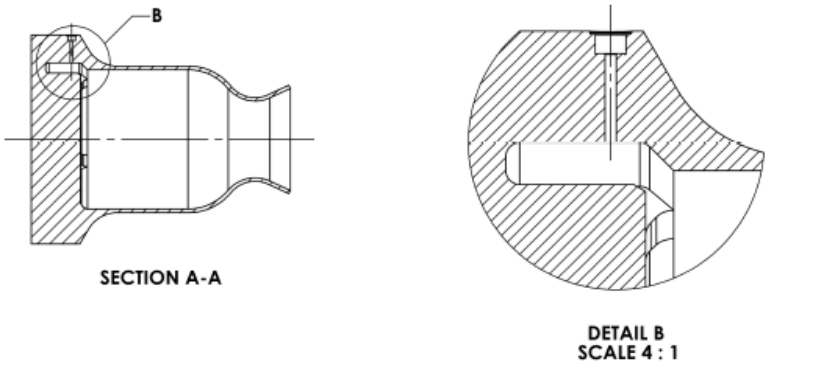

Figure 3: Schematic of an acoustic sense-line configuration branching from an acoustic cavity attached to the injection plate of a fictional liquid rocket engine.

from elevated temperatures. This introduces further discrepancies between the measured pressure and the desired pressure measurement of combustion instabilities in the reaction chamber.

A schematic of an example sense-line is shown in Figure 4. Sense-lines comprise an area-contraction followed by an extension tube. The area-contraction is located between points 1 and 2 with the extension tube extending to the right of this location with some length L and area S_2. The acoustic cavity, or the combustion chamber, is located to the left of the area-contraction and has some larger area S_1. By obtaining the acoustic response of a simulated sense-line and extension tube, the acoustic response of the area-contraction may be obtained in the lab. This will allow an engineer to correct the time-domain pressure-history measurements, taken using a sense-line, yielding an accurate estimate of the pressure history in an unstable combustor. Furthermore, models of the acoustic response of sense-lines and area-contractions can be developed based upon the measured data to aid in the prediction of combustion instabilities during the initial design phase.

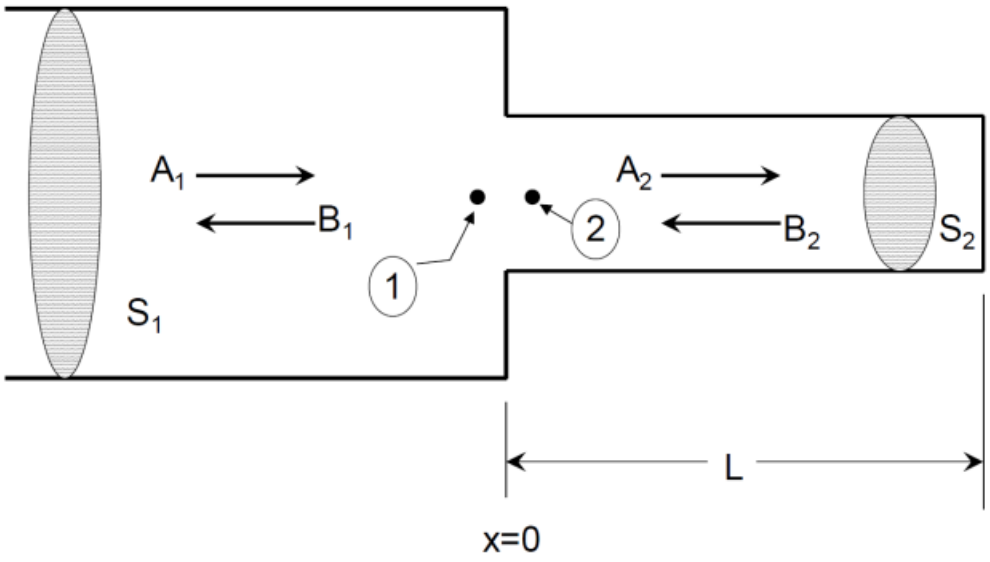

Figure 4: Area-contraction and sense-line combination where the area-contraction is located at x=0 and the sense-line is of length L with an area of S_2.

This work seeks to expand the knowledge base of acoustically compact area-contractions and sense-lines by experimentally recording acoustic response measurements to a range of frequencies, area-contraction ratios, acoustic velocity amplitudes, and sense-line area-contraction ratios via the use of an impedance tube. At present, these data are only sparsely available in the literature and often under conditions not appropriate to the combustion systems under consideration.[24-26]

The following chapter presents the background and theory pertaining to combustion instabilities, definitions of important acoustic parameters, the nonlinear acoustic response of area-contractions and the associated dampening mechanism, and previous observations of dependence on acoustic velocity amplitude of various geometries. The later chapters present a literature review, experimental setup, data reduction process, results and discussion, and final conclusions.

Chapter 2

Background and Theory

This chapter presents some background and theory of combustion instabilities, their detection, an acoustic model and parameters used in characterizing sense-line nonlinear acoustic response, and the dampening mechanism involved in area-changes.

Combustion instabilities are caused by a coupling between the dynamic heat release of combustion and the natural acoustic modes of the combustor. In reacting flows, the potential exists for a coupling between acoustic, vortical, and/or entropy oscillations and the combustion heat release process resulting in large heat release, acoustic pressure, and acoustic velocity oscillations. Therefore, acoustic oscillations lead to heat release oscillations, which tend to amplify the acoustic oscillations thus completing the cycle. According to this feedback loop, the amplitude of the acoustic oscillations continues to build until losses offset the driving of the system. The degree of amplification, if any, depends on the magnitude of the linear and nonlinear acoustic losses in the system. Eq. (1), the Rayleigh criterion[27], is an expression for the system gain G, which is the difference between the net system driving and damping.

$$\underbrace{\int_t \iiint_V p'(x,t)q'(x,t)dVdt}_{\text{term 1: driving}} - \underbrace{\int_t \int_{V,S} \Psi(x,t)}_{\text{term 2: damping}} = G \tag{1}$$

The gain G is negative or zero for a stable system and positive for an unstable system. Term 1 represents the heat release coupled driving oscillations and the acoustic pressure integrated over the combustion zone. Term 1 indicates that the driving is positive when the phase between the

acoustic pressure and heat release oscillations is around $\pm\frac{\pi}{2}$. This means that energy is added to the acoustic-field when this intermittent energy addition through heat release oscillations is within the phase limit of the acoustic pressure oscillations.[27] The damping term or term 2, is integrated over either the volume and/or surface of the net system depending on if the losses are assumed to occur within the fluid volume or at the boundaries of the system . When damping and driving are equivalent, the system is considered to be at its limit cycle. Detection of combustion instabilities has been shown to be possible since combustion instabilities in and of themselves are a coupling of the heat release and natural acoustics of the combustor. This coupling allows for measurements of combustion instabilities via the use of acoustic pressure sensors. As previously mentioned, sense-lines can be an effective method for removing sensors from the harsh reacting environment of a combustor allowing for the safe detection of combustion instabilities. However, sense-lines have a natural nonlinear acoustic response that skews acoustic pressure measurements. The nonlinear acoustic response of area-changes has been previously demonstrated by several authors.

It was Sivian[28] who was the first to identify the nonlinear acoustic response of a circular orifice. Specifically, the resistance of the orifice scaled nonlinearly with the acoustic velocity amplitude. Sivian[28] also reported that the resistance becomes important at acoustic velocities around 0.5 m/s. Shortly thereafter, Ingard[29], reported observations similar to Sivian's, and Ingard and Labate[30] stating that the nonlinear acoustic effects in orifices were closely tied to the flow patterns around the orifice. In 1967, Ingard and Ising[31] demonstrated that the impedance of orifices were constant at low pressure amplitudes. However, the impedance has a relationship, similar to a square law, for higher driving pressures. Zinn[32] in 1970 presented a theoretical model for the nonlinear real part of the impedance, or the resistance, of an orifice that also incorporated a discharge coefficient that includes the acoustic effects of the vena contracta and various flow

coefficients. Johnston and Schmidt[33] in 1967 reported substantial discrepancies between results of experiments and linear acoustic model predictions in which they attempted to measure the reflection coefficient of an obstruction in a pipeline. This discrepancy was attributed to wall radiation losses in the pipe. Cummings[34] presented an expression for the impedance of tube terminations similar to the one used in this study. The impedance expression developed included the nonlinear effects of the acoustic velocity and steady mean flow effects. Both depend on the area ratio between the cross-sectional area of the main duct and the effective area of the orifice connected to that main duct. Cummings[34] also found that the total losses in the system are different when the flow was forced out of and into the orifice.

Observations[25, 28, 34] have shown that both orifices and sense-lines have a nonlinear acoustic response and form an area-contraction at the interface of an acoustic cavity or combustor. This loss mechanism in the outflow from an orifice or area-contraction can be explained by a viscous dampening or jetting effect.

Figure 5 shows incompressible flow streamlines for conditions of outflow and inflow through an abrupt area-contraction. Figure 5(a) suggests that the flow loses very little total energy as it flows through the nearly isentropic area-contraction from 1 to 2. However, this geometry causes an increase in velocity of the flow resulting in a transition from laminar to turbulent flow. The flow turbulence dissipates vastly more energy due to high velocity at the tube wall. Therefore, some energy loss may be associated with the flow into the area-contraction.

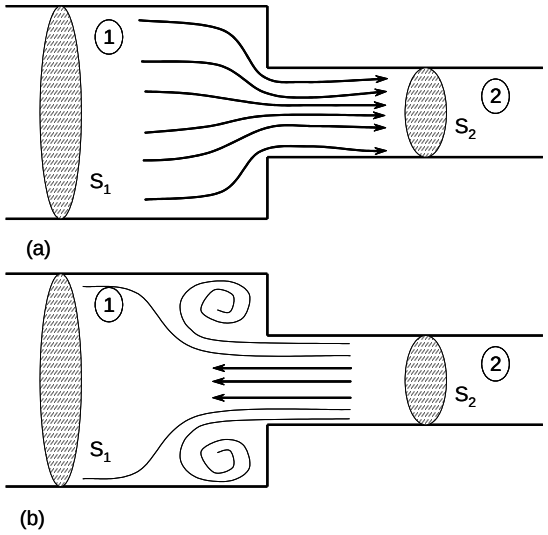

Figure 5: (a) Incompressible flow streamlines for an abrupt area-contraction with the flow direction going from region 1 to region 2. (b) Incompressible flow streamlines for an abrupt area-expansion with the flow direction from region 2 to region 1.[25]

Figure 5 (b) shows the flow path from regions 2 to 1 forms a turbulent jetting effect upon exiting the smaller tube. This jetting effect becomes turbulent at Reynolds numbers approaching 100 and higher[35]. This turbulent jetting flow from region 2, separates from the mouth of the area-contraction causing complex vortical structures to form, more commonly known as vortex shedding. Vortex shedding from the detached flow at the area-contraction leads to substantial energy loss and is the main culprit for the nonlinear acoustic response of orifices and area-contractions. In the case of steady mean flow from regions 2 to 1, the energy that was dissipated by the separated flow is proportional to $\left(V_2^{\,2} - V_1^{\,2}\right)/2$.[36]

Figure 6 illustrates the effects of low frequency acoustic velocity oscillations subjected to steady mean flow. For illustration purposes, the steady flow velocity is in the "forward" direction, i.e., flowing from the larger to the smaller area. In this case, isentropic flow conditions persist for the time marked $t_{forward}$, and separated conditions exist for the time marked $t_{reverse}$.

Because damping is associated with the separated flow, the amount of damping depends on the direction and the magnitude of the steady velocity relative to the acoustic velocity. However, when the flow direction is reversed, i.e., flow from smaller to larger area, jetting flow occurs over the entire cycle, and the damping is due only to the steady mean flow. This energy loss due to damping and net system resistance discussed above, can be obtained and represented mathematically by the complex reflection coefficient $\hat{R}$ and the complex acoustic impedance $\hat{Z}$.

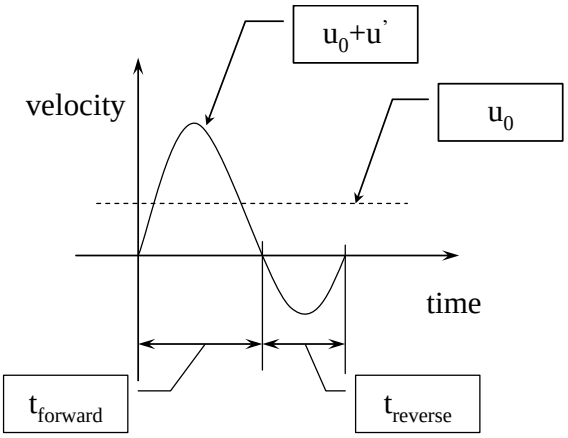

Figure 6. Steady flow imposed on an acoustic velocity oscillation vs. time.

The complex reflection coefficient is an indication of the amount of damping present at a specific frequency and is the ratio of the reflected and incident energies of the acoustic wave, assuming no energy is transmitted through radiation losses. Linear acoustic theory says that in the absence of damping, the system impedance will be purely imaginary and the magnitude of the complex reflection coefficient, measured at any location in the system, will be one because all the incident acoustic energy is perfectly reflected causing no energy loss. If any type of acoustic loss mechanism is present within the system, the acoustic impedance will have a real and imaginary component and the magnitude of the complex reflection coefficient will be less than one. In the situation where the reflection coefficient is zero, all the energy entering the measurement field is transferred out of the system completely or is perfectly absorbed.

The acoustic impedance has a real and imaginary part which is described by a resistance and reactance. The real part of the acoustic impedance acts as a resistive term, which is a

measure of the system's ability to dissipate or drive energy and is related to the damping present in a system, however, is not a measure of the damping. A positive real part of the impedance corresponds to the system's ability to dissipate energy while a negative real part of the impedance is the system's ability to drive energy. The resistance of a system can be increased by simply adding damping elements such as an area-contraction, valve, or internal geometry change. Conversely, a negative real part of the impedance is an indication of driving internal to the system and can only be achieved by adding driving elements such as purge air flow in the direction of the reflected wave or by adding acoustic speakers. The imaginary part of the impedance acts as the reactive term, or a measure of the systems potential to store energy and can be thought of as a mass-like inductance and spring-like capacitance. The inductance of the system can be increased by adding extensions of tubing or large element volumes such as an acoustic cavity, which adds mass to the system.

In acoustic response models, it is common to neglect nonlinear acoustic effects at low acoustic pressure amplitudes. For most applications, this assumption does not produce large errors and has the benefit of significantly simplifying calculations of the frequency response function of the system. However, it has been shown that certain geometries such as sudden area-changes, valves, and orifices, behave nonlinearly. These nonlinearities can only be neglected when the acoustic velocity amplitude is extremely small relative to the steady flow velocity, or in other words, never for systems without steady mean flow. In other words, the impedance of these geometries is dependent upon the acoustic velocity amplitude. Since purge air flow through sense-lines has been shown to alter the nonlinear acoustic response of area-contractions and orifices, flow terms must be accounted in the calculation of the acoustic impedance. This model needs to also account for the fact that over a small fraction of the oscillation period, the flow is

aligned with the same direction of the steady mean flow, and in the opposite direction for the other part of the cycle. The phase of the flow usually depends on the ratio of the acoustic velocity to the magnitude of the steady mean flow velocity. Thus, the order of dissipation will depend on the oscillation amplitude and the steady flow velocity component. For adequately high steady mean flow velocities, no flow reversal will occur. However, nonlinear acoustic effects will be dampened out well before this happens. Scarborough et. al.[37, 38] previously derived a model of the complex acoustic impedance describing a compact area-contraction including steady flow terms

$$\frac{Z}{\rho c} = \frac{p_1' - p_2'}{\rho c \cdot S_1 u_1'} = \frac{i\frac{\omega}{c}L_e}{S_1} + \left(\frac{u_0}{c} + \frac{|u_1'|}{2 \cdot c}\right)\frac{\left[\left(\frac{S_1}{S_2}\right)^2 + K_L - 1\right]}{S_1}, \tag{2}$$

which indicates that the real part of the acoustic impedance depends on both the acoustic velocity amplitude and the steady flow velocity, as well as the squared area ratio.

Linear acoustic theory says that in the absence of damping the phase of the acoustic impedance measured just upstream of the area-contraction must be $\pm\frac{\pi}{2}$. This is because the acoustic velocity and pressure are always 90 degrees out of phase with each other resulting in no dissipation of acoustic intensity. When a damping element is present in a system, the phase between the acoustic pressure and velocity will shift towards zero degrees depending on the amount of damping present in the system.

Based upon the theory above, high acoustic velocity amplitude at the area-contraction leads to large nonlinear acoustic damping. Therefore, driving frequencies leading to high

acoustic velocity amplitudes at the area-contraction are of interest. Assuming the sense-line closely approximates an open-closed tube, the anti-resonances and resonances are given by

$$f = \frac{nc}{2L} \tag{3}$$

where $n = 1, 2, 3, \ldots$ and

$$f = \frac{(2n+1)c}{4L} \tag{4}$$

where $n = 1, 2, 3, \ldots$, respectively.

High acoustic velocity amplitudes and acoustic damping is expected at the area-contraction for driving frequencies calculated using Eq. (4). Conversely, damping is expected to be low for frequencies calculated outside the resonant frequencies of the sense-line.

The flow behavior of an area-change is complex and depends on the acoustic and steady flow velocity through the area-change. Figure 5, a schematic representation of the flow through an area-change, demonstrates that the losses for case (b) are much greater than those in case (a) with the same flow velocity due to the presence of the recirculation zones. Since the pressure on either side of the area contraction are nearly equal during the jetting outflow process, flow kinetic energy and acoustic energy is dissipated. To characterize the nonlinear acoustic response of area-changes outside of a combusting environment, the area-change must be subjected to a driving element such as acoustic forcing by an electronic speaker. In this investigation, a multiple-microphone impedance tube, complete with electronic acoustic speakers as the driving element, was used to measure the acoustic response of sense lines, extension tubes, and area-changes.

An effective tool for characterizing the acoustic response of various geometries, materials, and components is the impedance tube. An impedance tube is comprised of a main duct with some inner diameter and length, an acoustic driving source usually placed at one end of the main duct, a location to install any sample of interest usually on the opposing end of the driving source, and two or more sensors arranged along the sidewall of the main duct. The acoustic drivers generate a standing sinusoidal pressure wave of some known frequency and amplitude that propagates down the main duct, interacts with the sample of interest, and returns with a modified amplitude and phase. Some impedance tube measurement techniques include; the multiple-microphone method, single microphone method, and the standing wave ratio method. Some sensor types include; piezoelectric pressure transducers, microphones, and microflowns. Some driving methods include; pure tone excitation, pseudo-random noise excitation, and random noise excitation. In post processing, the measurements obtained in an impedance tube can be converted from the time-domain to the frequency domain allowing the user to identify natural acoustic features of the impedance tube or of the sample of interest with high-accuracy.

The next chapter describes impedance tube best practices and measurement techniques available in the literature. This survey is followed by a review of the available literature to identify works that have characterized the acoustic response of various geometries known to exhibit acoustic nonlinearities. This is done to identify significant gaps in the work that has been done on acoustically compact geometries such as area-changes.

Chapter 3

Impedance Tube Best Practices and Literature Review

Several impedance tube measurement methods and driving techniques have been used over the last century to characterize the linear and nonlinear acoustic response of materials and geometries. Each of these methods are specifically designed to obtain the highest accuracy data possible based upon imposed experimental restrictions, such as geometric confinement and time considerations. The literature has been reviewed in depth below for various measurement methods used in conjunction with an impedance tube. The reason for this separate and more in-depth literature review, is for taking into consideration past lessons learned and best practices in the design of an impedance tube since one goal of this study is to obtain high-accuracy and high-resolution acoustic response data. It is also to identify the most accurate method for obtaining acoustic pressure measurements using an impedance tube with the most accurate driving method possible. This chapter includes a comprehensive review of the available literature to (1) obtain impedance tube best practices and to compare measurement method accuracy, and (2) to identify significant gaps in the literature.

3.1 A Comparison of Impedance Tube Measurement and Driving Methods

Several authors reviewed below, have focused on implementing potential improvements to the single microphone, two-microphone, and the multipoint methods, or more widely known as the multiple-microphone method. Another purpose of these articles was to identify

measurement method accuracy and compare their data acquisition time with various methods of acoustic driving.

Most recently, De Bree[39-41], has employed the use of a new method for measuring the acoustic behavior of sound absorbing materials in an impedance tube. This method makes use of a novel particle velocity sensor called a Microflown, which has been used in other works[41, 42]. This method has also been compared to other, more well-established impedance tube measurement methods such as the standing wave ratio method invented by Fahy[43], and the transfer function method designed by Chung and Blazer[44]. The standing wave ratio method utilizes the ratio between the maximum and minimum pressure in an impedance tube, removing the need for calibration of the microphones. However, this method is prone to errors in measuring the standing wave minima and maxima. It was found that a combination of microphones and Microflown's can provide direct information about the acoustical properties of materials or geometries, however is prone to bias errors. It was also found that for narrow tubes, the visco-thermal effects on the wave propagation are important.

Likewise, the single microphone method used by Fahy[43] and Chu[45, 46] were used in an attempt to determine measurement capabilities in a restrictive environment. The multiple frequency driving version of the multiple-microphone method, or pure tone excitation method utilized by Chu[47], was included in this investigation as an extension of the multiple-microphone method. Chu[46] also utilized a pseudo-random noise driving method, which generates a combination of discrete frequencies, each at a selected phase and amplitude. Out of each of these driving methods, it was found that the pure tone excitation driving method yielded the highest accuracy data with the least measurement error.

Schurer[42] compared the single microphone method with the standing wave ratio method by measuring horn input impedance. It was found that Microflowns allow for faster and easier measurements of acoustic properties, however with less accuracy.

Jones[48] article was to compare each of the normal incidence acoustic impedance measurement methods in use at the NASA Langley Research Center for accuracy, consistency, and efficiency. Specifically, three impedance tube measurement methods were explored with three varying driving conditions. The measurement methods were the multiple-microphone, the two-microphone, and the single microphone methods. The driving conditions were random noise, pseudo-random noise, and pure tone excitation. Based upon method accuracy and amount of time needed to conduct the experiment, it was found that the single microphone method was accurate with a single discrete frequency source, but was still found to be less accurate compared to the multiple-microphone method with the same driving method. Whereas the single microphone method lacks in accuracy in a broad frequency range, the multiple-microphone method minimizes the degradation in signal to noise ratio in order to measure a potentially infinite frequency range. Overall, it was found that the multiple-microphone method yields the highest accuracy however, it is the most time-consuming method.

Seybert[49] used the two-microphone method in conjunction with random frequency excitation to characterize normal acoustic properties in a tube, without steady mean flow. Three test cases were looked at; one with a randomly excited open-ended tube, a rigidly terminated tube, and a prototype muffler to compare experimental results with the standing wave ratio method. It was found that the two-microphone random-excitation method was less time consuming and thus less labor intensive as compared with the standing wave ratio method. The data collection process took only seven seconds of continuous data to reproduce the desired

frequency spectrum of 0 to 3500 Hz, whereas the pure tone excitation method would have taken several minutes. However, it was found that the two-microphone random-excitation method can cause an increase in random and bias errors in the data and thus would not be an appropriate choice for high-accuracy data acquisition. Seybert did show potential in the two-microphone method for obtaining high-accuracy low frequency data.

Chu[47] also improved and compared three existing methods for measuring the acoustical properties of materials using an impedance tube. Three test materials were used; carpet, foam, and resonant absorber, in conjunction with an improved version of the standing wave ratio method with pure-tone excitation, an improved version of the transfer-function method with pure-tone excitation, and the least-squares method with broad-band excitation. It was found that the improved version of the transfer-function method with pure-tone excitation is simple and very accurate, but requires the correct sensor spacing for each individual frequency. This method is better than the standing wave ratio method mainly due to the freedom of having less accurate sensor placement. The least-squares method with broad-band excitation is much faster than the other two methods, but yields less accuracy.

Jang[50] compared several methods for measuring acoustic properties in the presence of steady mean flow. The author described how the standing wave ratio method can be, in some cases, more accurate than the two-microphone method, but with a drawback. It can be very time consuming especially across a wide range of frequencies. The two-microphone method, on the other hand, can be just as accurate, but conducted in a fraction of the time that the standing wave ratio method would require.

3.2 Sensitivity Analyses and Error in Impedance Tube Measurement Methods

Several articles in the literature considered the error associated with measuring acoustic parameters and identified best practices used in various measurement techniques, such as proper sensor spacing, proper impedance tube length/diameter considerations, and the avoidance of acoustic noise.

Katz[51], looked at errors relevant to microphone and sample locations using the two-microphone method, specifically using the measured transfer function between two microphones. The author investigates and incorporates previously known "best practices" for measuring acoustic properties within a duct as noted by the ASTM[52] standard. According to these standards, the diameter of a working Impedance tube should be less than $0.586\frac{c}{f_{\max}}$ where $f_{\max}$ is the maximum frequency desired by the investigator. Another method of best practices that the author incorporates into their work, suggested by the ASTM standard, is to not place the reference transducer closer than one duct diameter from the sample location. This is to avoid the effects of exponentially decaying evanescent wave forms reflecting from the sample. Otherwise, the pressure measurements obtained would be less accurate due to increased noise. It is stated that the optimal sensor spacing for minimal amount of error is defined by $s < \frac{c}{2 f_{center}}$, or is less than the resonant frequency of the closed-closed duct. It was also found that by varying sensor location from the nominal sensor position, the induced error on the reflection and absorption coefficients of a sample of typical acoustically dense foam, changed on the order of the location

mismatch error. The author did not provide experimental data that reproduced the accuracy of their method.

Chu[45], also used the single microphone method with a periodic pseudorandom noise driving source. One advantage to the use of the single microphone method is elimination of a calibration step. The elimination of the calibration step negates any error associated with phase-mismatching. However, the accuracy gained by eliminating the calibration step is heavily outweighed by measurement error in the method itself. On the other hand, Chu[45] was able to obtain a simple equation that calculates nominal sensor spacing, by using data acquired from various sensor locations, based upon the maximum desired test frequency, $s = 0.7\frac{c}{2f_{\max}}$. This equation is consistent with the one found by Katz[51]. It was also suggested by this author that a longer spacing from the reference transducer in the two-microphone method, yields higher accuracy data at low frequencies, which is consistent with theory behind the multiple-microphone method. Though the single microphone method can drastically improve testing time, it lacks the accuracy needed to take high-quality low-error acoustic response data.

Boden and Abom[53] studied the error associated with the two-microphone method for measuring acoustic properties within ducts. Their goal was to discuss and analyze the influence of all types of error associated with the two-microphone method developed by Chung and Blaser[44]. One source of error was the error due to microphone spacing. Another was the measurement error below 400 Hz, which was found to be due to low signal to noise ratios. The final source of error was induced error found in calculated quantities. The authors introduced a slight phase and amplitude error in the measured quantities and then proceeded to calculate the reflection coefficient and acoustic impedance via the transfer function method. Random errors

induced in the calculated quantities were chosen to be 1% in the magnitude and phase which is the error magnitude expected in testing. Errors in the sensor spacing's were also chosen to be of 1%. This was done to analyze the sensitivity of the calculations to errors in the input data. In conclusion, to minimize bias errors, the maximum duct length that should be used is between five and ten duct diameters long, the source end of the duct should be as non-reflective as possible, and the reference transducer should be placed as close to, but a minimum of one duct diameter away from the sample location to avoid the influence of near field effects. To obtain relative error of less than 1% of transducer spacing, a spacing of greater than 50 mm or 1.97 inches is required otherwise length errors might dominate. Finally, it was found that to avoid large errors in sensitivity of input data, the two-microphone method should only be used in the range of $0.1\pi < ks < 0.8\pi$ for two microphones with optimal spacing s.

Boden and Abom[54], again looked at the error associated with the two-microphone method for measuring acoustic properties within ducts subjected to steady mean flow. Error related to neglected attenuation, non-ideal microphones, and flow noise were considered in this investigation. It was found that neglecting acoustic attenuation between transducers, or the energy lost by sound propagation in a medium, leads to a low frequency limit. At low frequencies, there is an increase in acoustic energy loss when subjected to steady mean flow. This effectively causes large bias error due to low signal to noise ratio at low frequencies with high flow rates. If a sufficiently high sound pressure level is not produced compared to the flow noise level in the duct, a large bias error will dominate.

Scarborough[25] analyzed measurement error in the complex reflection coefficient by taking the total derivative of the complex reflection coefficient with respect to the complex pressure ratio as measured using the multiple-microphone method. An initial measurement error

could be assumed and applied to this total differential to obtain the total error in the measurement of the pressure ratio. This allows the author to identify practical sensor spacings for frequency ranges with minimal measurement error using the multiple-microphone methods.

The authors above have explored the use of the single microphone method, the transfer function method, the standing wave ratio method, the multiple-microphone method, and the two-microphone method. Each measurement method can then be conducted using varying methods for driving including pure tone excitation, pseudo-random noise excitation, and broad-band excitation. It has been shown that by far the most accurate measurement technique in combination with driving method is the multiple-microphone method in conjunction with pure tone excitation, which are the measurement and driving techniques chosen for this current study. The benefits of this method are carefully laid out in.[41, 48] It has also been shown that certain standards, lessons learned, and deficiencies in the data should be employed in the data collection process. Several other design parameters that are outline above are discussed and used in the experimental setup of this investigation.

3.3 Significant Gaps in the Acoustic Response Data of Area-Contractions

Several significant gaps exist in the available acoustic response data for abrupt area-contractions and sense-lines. While several papers have been published on the effects of steady mean flow on the acoustic response of orifices, perforated plates, and sound absorbing materials, the data on area-contractions and sense-lines is almost nonexistent. Not a single study was found in the available literature on the specific acoustic response of area-contractions with high-resolution data acquisition in the frequency range of interest other than previous works conducted

by Scarborough[25]. This section surveys the literature for works that have looked at the acoustic response of various geometries with and without steady mean flow.

The acoustic response of orifices was one of the most widely studied geometries in the literature. Of the 16 journal articles considered [28, 34, 55-65], two studies [57, 60], focused solely on the linear behavior of orifices in the presence of an acoustic field. The remaining articles concentrated on the nonlinear acoustic response of orifices, with some discussion of linear behavior in the presence of steady mean flow. In almost all the studies, measurements were made for isolated frequencies or over sparsely populated frequency ranges, sometimes with a frequency step of 100 Hz to over 1 kHz.

Several articles [55, 57-62], included the effects of steady mean flow and concluded that without steady mean flow the acoustic impedance of an orifice is inherently nonlinear and therefore, cannot be modeled by linear acoustic theory. However, as references [55, 57] show, orifice resistance is directly proportional to the grazing flow velocity at sufficiently high, steady flow velocities. Several studies present models for orifices in grazing flow, but do not provide experimental data to confirm their assertions.

The literature indicates that data and models are needed for the following conditions to fill some of the gaps in the knowledge base on the acoustic response of orifices; (1) high sound pressure levels greater than 150 dB to provide data for the rocket community, (2) high frequency resolution at or less than frequency spacing's of 10 Hz for acoustic response data, and (3) complete acoustic impedance data as a function of acoustic velocity amplitude describing the systems nonlinearities.

Perforated plate acoustic response was the second most extensively studied acoustic element [41, 66-74]. Of the 11 journal articles considered, four [66, 70, 73, 75] studied the effects of bias

flow, five [68-71, 73]studied the effects of grazing flow, and one [73] studied the effects of grazing and bias flow together. None characterized the nonlinear acoustic response of perforated plates without steady mean flow. Perforated plate acoustic response was also studied for frequencies as high as 10 kHz, but lacked the relevant data at frequencies where plane waves form below 1500 Hz. However, many studies [41, 66, 68, 70] focused on the frequency range of 0 to 1000 Hz with broad frequency spacing between tests. Five studies [41, 66, 68, 70, 71] omit low frequency data from 0 to 300 Hz completely.

Perforated plate acoustic response experimental data and models are needed for the following conditions: (1) high-resolution high-accuracy frequency response data for frequencies under 300 Hz, (2) grazing and bias flow studies from Mach 0 to 0.3, (3) and a high-resolution overall frequency range of 0 to 1500 Hz with step sizes at or less that 10Hz.

Area-contraction studies[25, 44, 76-78] are not nearly as pervasive in the literature as orifices and perforated plates. Only a single study, conducted by Lambert and Steinbrueck[78], looked at the effects of bias flow in area-contractions. While Simonich[76], looked at the effects of grazing flow. The only work found, in the available literature, on area-contractions without steady mean flow was that of the dissertation work conducted by Scarborough 2010 [25], who looked at various area-contraction lengths and diameters to characterize their nonlinear acoustic response.

Two journal articles were found on area-expansions [79, 80]. Dupere and Dowling[79] conducted bias flow studies for Mach numbers between 0.015 and 0.1. Similarly, Gikadi[80] conducted studies at Mach 0.2.

Several significant gaps exist in the available acoustic response data for area-contractions with and without steady mean flow. While numerous papers have been published on the effects

of the nonlinear acoustic response of orifices, perforated plates, and sound absorbing materials, the data on area-contractions is almost nonexistent. Based upon the described deficiencies in the available literature, it is the goal of this article to create a comprehensive log of area-contraction acoustic response data over a wide range of (1) driving frequencies with a frequency resolution of less than 10Hz, (2) driving acoustic pressure and velocity amplitudes at the area-contraction with and without steady mean flow, and (3) to compile a complete collection of acoustic impedance data as a function of acoustic velocity amplitudes. Since longitudinal combustion instabilities in modern combustors such as gas turbine engines or liquid rocket engines present themselves as plane waves in the range of 100 Hz to 1000 Hz[25] and the broad literature review given above is consistently missing data at low frequencies up to 1500 Hz, the frequency range of interest for this work was chosen to be 100 Hz to 1500 Hz. This frequency range allowed for the initial design and optimization of the impedance tube used in this study.

Chapter 4

Experimental Facility

This chapter makes use of the best practices and design criteria, found in the available literature, for constructing a multiple-microphone method impedance tube. The data acquisition and control of the impedance tube is also discussed.

The objective of this study was to measure the nonlinear acoustic response of simulated sense-lines with four area-contraction ratios and a single sense-line length over a wide range of acoustic velocity amplitudes and frequencies. A multiple-microphone impedance tube was constructed for this investigation. The multiple-microphone method is based on the two-microphone method developed by Munjal, Chung and Blaser[44, 81]. In the two-microphone method, the complex reflection coefficient $\hat{R}$, neglecting steady mean flow, is calculated from the Fourier transformed acoustic pressure-history measurements as follows

$$\hat{R} = \frac{e^{ikx_1} - \frac{\hat{p}_1}{\hat{p}_i} e^{ikx_i}}{\frac{\hat{p}_1}{\hat{p}_i} e^{-ikx_i} - e^{-ik_i x_1}} \tag{5}$$

The complex reflection coefficient is used in this study to identify frequency regions with significant damping due to the acoustic sense-line. The dimensionless form $\hat{\zeta}$ of the acoustic impedance $\hat{Z}$, as defined by Blackstock[23], is obtained from measurements of the reflection coefficient using

$$\hat{\zeta} = \frac{S\,\hat{Z}}{\rho c_o} = \frac{1+\hat{R}}{1-\hat{R}} \tag{6}$$

The multiple-microphone method assumes that longitudinal, plane acoustic waves propagate in the duct without higher order modes. Therefore, the maximum duct diameter is limited by the cutoff frequency of the first higher order mode, which according to Blackstock[23] is given by $f = \frac{nc}{2D}$. This study found that unacceptable damping was present for duct diameters less than 50.8 mm. Therefore, using this duct diameter the first cutoff frequency was found to be 3376 Hz, which was more than twice the maximum frequency of interest, 1500 Hz. In order to minimize wall radiation losses, the pipe walls were chosen to be 25.4 mm thick.

The length of the impedance tube was minimized to limit the number of resonances and anti-resonances within the frequency range of interest. Approximating the impedance tube as a rigid, closed-closed pipe, the anti-resonances and resonances are given by equations Eqs. (7) and (8)

$$f_{\text{res}} = \frac{(2n-1)c}{4L} \tag{7}$$

and

$$f_{\text{anti-res}} = \frac{nc}{2L}\ , \tag{8}$$

respectively, where $n = 1, 2, 3, \ldots$. These equations indicate the shorter the pipe length, the fewer resonances and anti-resonance will occur in the frequency range of interest. Given the lowest frequency of interest and the allowable measurement error, a sensitivity analysis was used as a verification tool in determining the minimum spacing between the two measurement sensors.

Results for this sensitivity analysis are presented and discussed near the end of this chapter. Increasing the sensor spacing would theoretically decrease the measurement error, but simultaneously require the length of the impedance tube to increase, which as discussed above has the undesirable effect of increasing the number of resonances and anti-resonances within the frequency range of interest. For a minimum frequency of 100 Hz and an allowable error of 2%, the sensor spacing was found to be 203.2 mm. In addition, Boden and Abom[53] suggest the pressure sensors be no closer than one duct diameter from the sample location or the driving speakers. Therefore, the minimum impedance tube length is two duct diameters plus the maximum microphone spacing, which for the 50.8 mm diameter impedance tube used in this study gives a length of 304.8 mm. As a rule of thumb, several authors recommend the overall impedance tube length be between five and ten duct diameters.[52, 53] The length of the impedance tube used in this study was 355.6 mm, which is seven duct diameters.

While long sensor spacing yields more accurate results at low frequencies, the reflection coefficient is indeterminate for $f = \frac{nc}{2(L_i - L_1)}$ neglecting steady flow terms. For a sensor spacing of 203.2 mm, the indeterminate frequency is 844 Hz. Therefore, a second pair of sensors was required for measurements ranging from 450 Hz to 1500 Hz. It is suggested by Boden and Abom[53] that the minimum sensor spacing be no less than 50 mm to maintain a relative error between sensors of less than 1% or the influence of length errors may begin to dominate. The data from these two sensor spacings was then "stitched" together in post-processing. A sensitivity analysis in conjunction with experimental measurements was conducted to determine the optimal sensor spacing, optimal distances from the sample location, and optimal distances

from the driving location based on the minimum and maximum spacings discussed above. This analysis and these data are discussed after the data reduction process in Chapter 5.

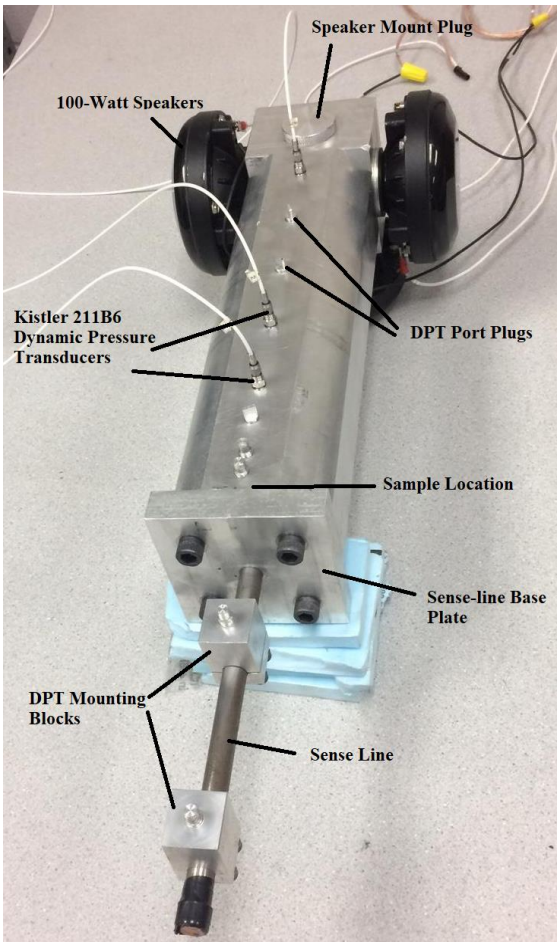

Figure 7: Sense-line attached to the fully functional impedance tube.

Figure 7 and Figure 8 show a photograph and schematic, respectively, of the developed impedance tube. A speaker mounting block (SMB) is shown attached to the aft end of the standing wave tube (SWT). The SMB is sealed to the SWT with an O-ring and bolted in place. As shown, three speakers were installed in the SMB. Also shown in the SMB are two venting ports, one on back and one on top, for use during flow testing. For this study, solid aluminum plugs were installed in these ports to provide a rigid termination. The inner diameter of the SMB matched the inner diameter of the SWT to eliminate internal area-changes and discontinuities. Also shown in Figure 7, are three dynamic pressure transducers (DPTs) mounted in the sensor ports. Solid sensor plugs were installed in the other ports flush with the inner SWT surface. The SWT is a smooth continuous tube 304.8 mm long, by a 50.8 mm inner diameter and a 95.25 mm outer diameter. The wall thickness was milled down to 20.828 mm to create a flat surface on all four sides of the SWT. This flat outer surface allows the DPTs to seal flush with the outer surface as

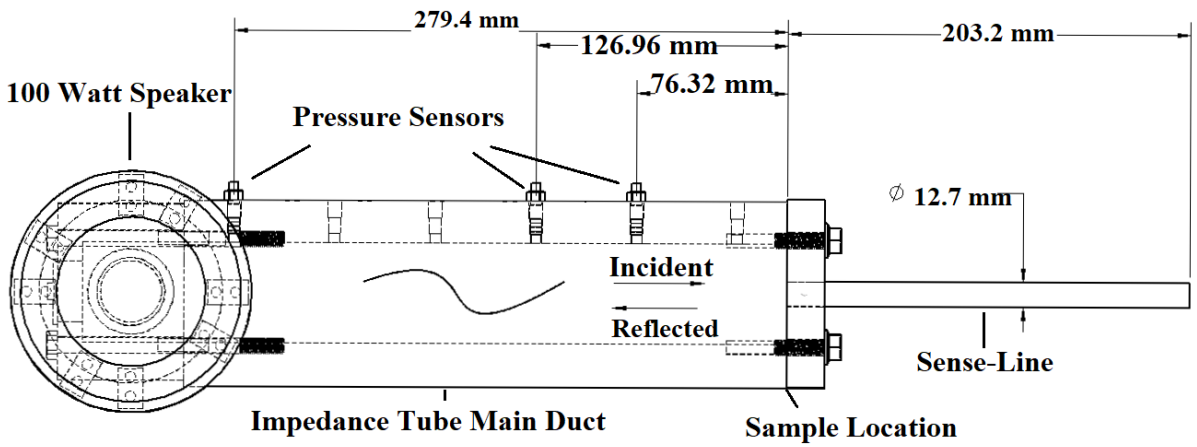

Figure 8. Schematic of the measurement head, simulated sense-line, acoustic sensors and hypothetical incident, reflected and transmitted acoustic waves.

well as the inner surface of the SWT. Six DPT ports were machined into the wall of the SWT with known distances from the sample location. This was done to experimentally determine the effects of sensor spacing and distance from the sample location.

As shown, one of the tested sense-lines was installed at the sample location, which was O-ring sealed and bolted to the SWT at the location indicated. For these experiments, the sense-line was rigidly terminated with a tube cap. Also shown attached to the sense-line are two transducer mounting blocks (TMB). For some experiments, DPTs were installed in these blocks to obtain dynamic pressure histories in the sense-line.

The following section describes the data acquisition and control process for the impedance tube described above.

4.1 Data Acquisition and Control

This section describes the data acquisition and control system used in the described experiments. The LabView graphical user control interface, shown in Figure 9**,** allows the user to control the start, stop, and resolution of the driving amplitude and frequency, and data file name.

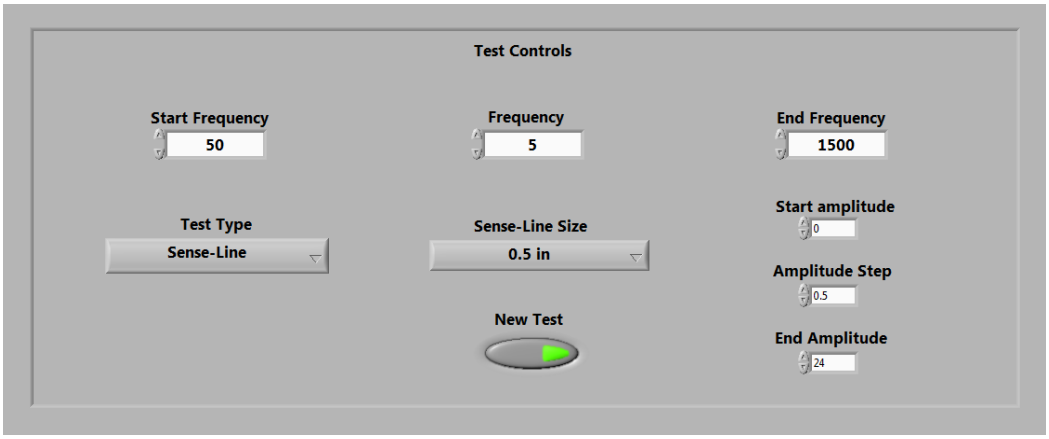

Figure 9. LabView control interface for National Instruments c-DAQ.

A control diagram describing the data acquisition process in detail is shown in Figure 9. From the moment the user runs the LabView program, a National Instruments Compact-DAQ relays the beginning mono-frequency driving signal to two Pyle PTA 1000 two-channel power amplifiers. The c-DAQ generates a voltage signal, which the power amplifier outputs as a constant RMS power signal. The amplifiers then relay an amplified driving wattage signal to the three 100-Watt speakers, which generates a high-amplitude standing wave inside of the SWT. The LabView data acquisition program allows a time delay of 250 milliseconds to allow the pressure field to reach steady state. At the end of the time delay, the c-DAQ begins to record voltage history measurements from three Kistler 211B6 DPTs. The signal from the sensors is amplified using a Kistler 5134B four-channel power amplifier with low-pass filtering below 10 kHz and high-pass filtering above 5 Hz using a built-in anti-aliasing band-pass filter. The

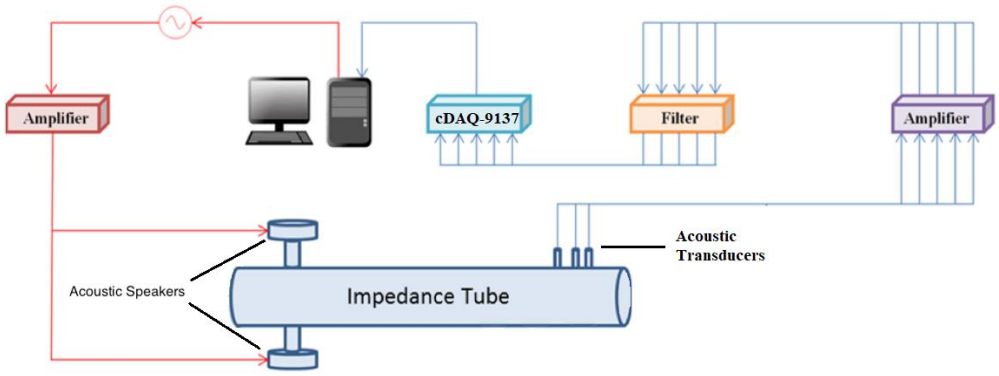

Figure 10. Control diagram of the impedance tube data acquisition process.

amplified and filtered signal is then relayed to an NI9234 voltage input module, passed through the c-DAQ card, and saved by the computer to a multi-array global variable input excel spreadsheet. The voltage history signal is sampled at the maximum sampling rate of the NI9234 voltage input module of 51,200 Hz for one second recording 25,600 samples. Once sampling is complete, driving continues for an additional 100 milliseconds. After driving stops, there is another 100-millisecond gap before proceeding to the next frequency.

Two different tests were conducted during this study. In one, the amplitude of the driving signal voltage was set through the LabView interface and the frequency of the driving signal was varied. For each frequency-varying test, the DSW amplitude was set and the speakers were driven at discrete frequencies every 5 Hz from 100 Hz up to 1500 Hz. For each DSW varying test, the DSW was varied from the highest possible mechanical output of the speakers, limited only by mechanical screeching of the speaker diaphragm, down to an output of zero. A sufficient number of samples in between the maximum driving output and no output were chosen to produce enough data points to be considered “high-resolution”.

The following section discusses how steady mean flow is introduced into the impedance tube for flow experiments.

4.2 Introducing of Steady Mean Flow into the Impedance Tube

This section discusses how steady mean flow is applied in the forward and reverse direction of the impedance tube. Also discussed is the equipment used and measurement methods of the volumetric flow rate.

Compressed air is supplied to steady mean flow tests in the laboratory from a 1034 kPa shop air compressor and storage tank. The flow system shown in Figure 11 was used to provide a regulated, metered steady flow of air to the area-contraction. As shown, the air pressure was reduced to 420.58 kPa gauge using a pressure regulator positioned just downstream of a shut-off ball valve. The air flow rate and pressure drop were measured just upstream of a calibrated, choked, flow regulating orifice, which was attached directly to the "closed" end of the sense-line. Since the flow is choked at the orifice, this boundary is considered to be a rigid termination, or closed end, as far as the acoustics of the system are concerned. The air flow rate was measured using a rotameter with a 5% turndown accuracy capable of measurements as low as 0.283 m^3/hour in

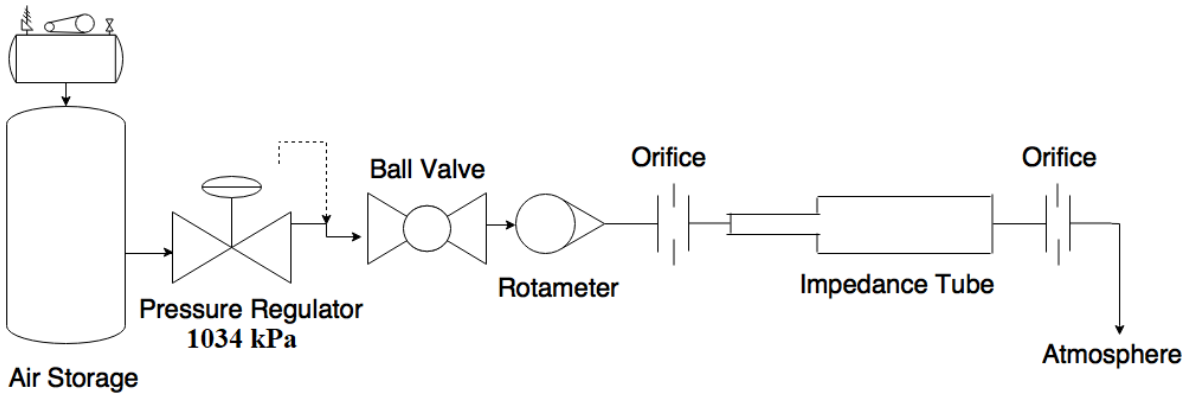

Figure 11. P&ID flow schematic for introduction of steady mean flow through orifice plate and sense-line/ impedance tube combination.

accuracy and as high as 0.849 m^3/minute. Several orifices were made for flow testing by drilling varying hole sizes into several pieces of 12.7 mm diameter circular pieces of shim stock. Air from the orifice flows down the length of the extension-tube, through the area-contraction, into the impedance tube, and finally, exits the impedance tube through specialized speaker plugs as shown in Figure 12. The flow can also be reversed to travel through the impedance tube, across the area-contraction, and exhaust through the extension-tube to atmosphere.

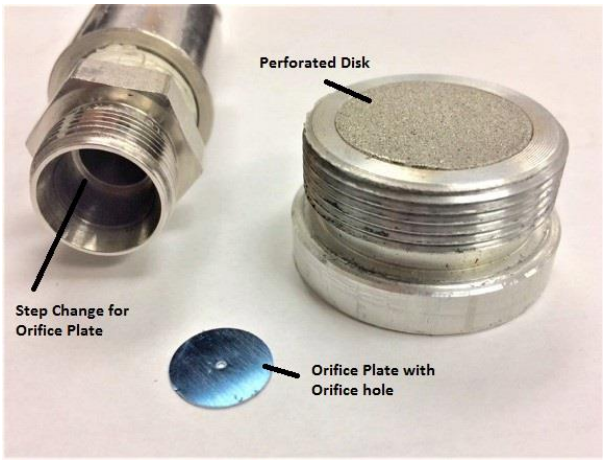

Figure 12. From left to right: orifice housing with internal step change, shim-stock laser-cut orifice, and speaker plug with perforated disc for free air flow.

The specialized speaker plugs were constructed to allow airflow to pass out of the impedance tube but also to appear as a mostly rigid end-condition. To determine if the perforated plugs had any effect on the frequency range of interest for frequency sweep tests, several tests were conducted with the perforated plugs and solid-walled plugs to identify any differences in the data. It was found that the perforated plugs caused no discernable difference in the frequency range of interest. These tests proved to be within repeatability error, which is discussed in a later section. A photograph of the orifice housing, an orifice, and a perforated plug are shown in Figure 12.

Chapter 5

Data Reduction Procedures

This section describes the data reduction process used in this study. A Brüel and Kjær (B&K) piston-phone type 4228, was used to verify DPT output. The piston-phone was factory calibrated to output a 250 Hz nominal sinusoidal waveform with a factory-calibrated SPL of 124.04 dB. Each sensor was placed in the adaptor port and inserted into the head of the piston-phone. The measured SPL of each sensor was then corrected for barometric pressure. The DPT output voltage amplitude was converted to a pressure history signal using

$$P_{measured} = \frac{V\left(6894.76\frac{Pa}{psi}\right)}{\left(S\frac{volts}{psi}\right)G_{amp}} \tag{9}$$

The measured sound pressure level (SPL) was computed using $SPL = 20\log_{10}\left(\frac{P_{measured}}{2E-5Pa}\right)$. The measured SPL was within $\pm 0.02\,dB$ of calibrated piston-phone SPL. The measured frequency of each DPT was within $\pm 0.01\,Hz$ of the calibrated piston-phone frequency.

The Fourier transform of each DPT's pressure history, using MATLAB's built-in Fast Fourier Transform (FFT). The scaled complex pressure amplitude was obtained from the Fourier transformed data using

$$\hat{p}_i = \frac{2\,conj\left\{FFT\left[p_i(t)\right]\right\}}{N_s} \tag{10}$$

The complex conjugate of the FFT appearing in Eq. (7) was taken because MATLAB's implementation of the FFT assumes the e^{iwt} time convention. However, in this study the e^{-iwt} time convention was used.

The RMS amplitude was obtained from the pressure amplitude using

$$Amp_{fft} = \sqrt{\sum_{\pm f} \left[\frac{|\hat{p}_i|}{\sqrt{2}} \right]^2} \tag{11}$$

where the summation was carried out over a frequency range of ± 20 Hz about the driving frequency. This amplitude was compared with the true RMS amplitude of the time domain signal. These values were found to be within 0.01% of each other over all frequencies tested.

The complex pressure amplitude from the FFT at the driving frequency was converted to the time domain using

$$p_{i,\text{recon}} = \frac{1}{2}\left[\hat{p}_i e^{-i\omega t} + conj\left(\hat{p}_i\right) e^{i\omega t} \right] \tag{12}$$

Figure 13 shows good agreement between the reconstructed and experimentally measured pressure histories for one driving frequency.

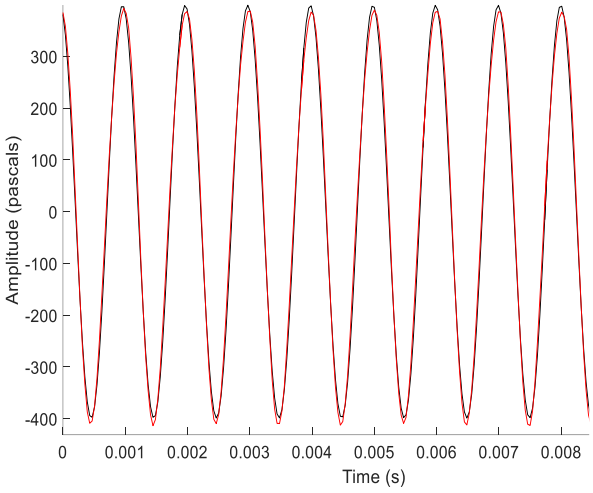

Figure 13. The reconstructed time domain signal (black) overlaid on the scaled original time domain signal (red).

5.1 Calibration Process

The multiple-microphone method requires accurate calibration of each DPT with respect to a reference DPT. Each DPT was installed in a calibration plate, which was then

mounted at the sample location, as shown in Figure 14. Plane acoustic waves were driven in the SWT at discrete frequencies over the entire frequency range of interest, and pressure histories for each DPT were recorded. The complex pressure amplitude at each frequency for each DPT was computed from these data. Pressure amplitude and phase correction factors relative to the reference DPT were computed from these complex pressure amplitudes as follows: $AF_{ref,i} = \left|\hat{p}_{ref}\right| / \left|\hat{p}_i\right|$ and $\delta\phi_{ref,i} = \phi_{ref} - \phi_i$. The corrected complex pressure amplitude for each DPT is then computed using

Figure 14. Microphones threaded into an end plate of the impedance tube used for calibration.

$$\hat{p}_{i,\text{corr}} = \hat{p}_i \left| AF_{ref,i} \right| e^{i\delta\phi_{ref,i}} \tag{13}$$

Having obtained the corrected pressure amplitudes, these values can be substituted into the specific complex reflection coefficient equation

$$\hat{R} = \frac{e^{ik_i x_1} - \dfrac{\hat{p}_{1,\text{corr}}}{\hat{p}_{3,\text{corr}}} e^{ik_i x_3}}{\dfrac{\hat{p}_{1,\text{corr}}}{\hat{p}_{3,\text{corr}}} e^{-ik_i x_3} - e^{-ik_i x_1}} \tag{14}$$

where k_i^+ and k_i^- are the steady flow wavenumbers found by solving the convective wave equation and represented as

$$k_i^+ = 2\pi f \Big/ c\left[1+M_{0,i}\left(\bar{n}_{V_0}\cdot\bar{n}_x\right)\right]$$
$$k_i^- = 2\pi f \Big/ c\left[1-M_{0,i}\left(\bar{n}_{V_0}\cdot\bar{n}_x\right)\right] \quad (15)$$

The dimensionless impedance can then be calculated using Eq. (6).

To demonstrate the effectiveness of the calibration procedure described above, a calibration was conducted to obtain amplitude and phase correction factors, as previously described. Next, a second "calibration test" was conducted to obtain a new set of pressure histories for each DPT. These uncorrected pressure histories are shown in Figure 15A Since all the DPTs are measuring the same pressure field, each measured pressure history should perfectly match. However, as the figure shows, there is a slight difference in the amplitude and phase of each measurement compared to the reference. The amplitude and phase correction factors were applied to the individual complex pressure amplitudes obtained from these pressure histories. These corrected complex pressure amplitudes were substituted into Eq. (11) to obtain reconstructed pressure histories, which are shown in Figure 15B. As the figure shows, there is good agreement between the corrected pressure histories.

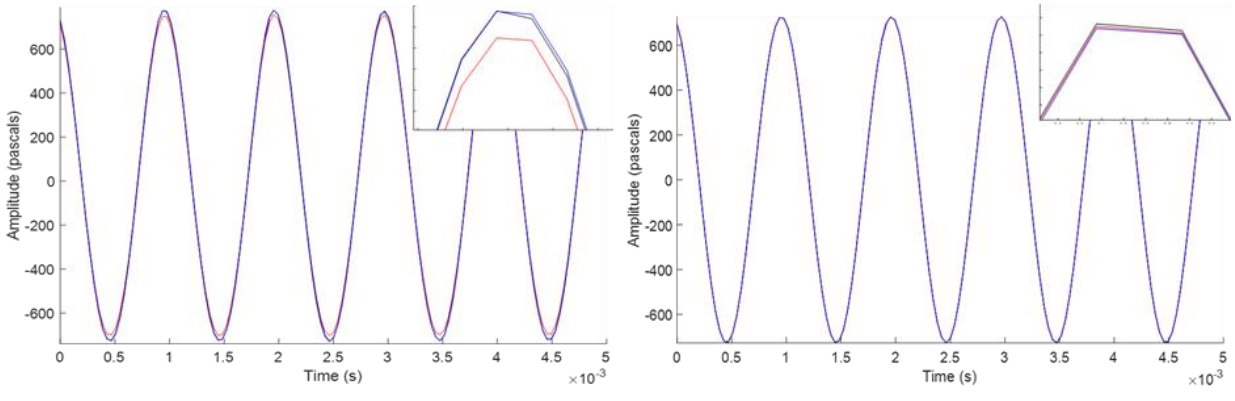

Figure 15. A) Uncorrected pressure histories versus time for each DPT. B) Corrected pressure histories versus time for each DPT.

5.2 Complex Amplitude and Acoustic Velocity

The acoustic pressure and velocity distributions in the tube are given by Eq. (16) and Eq. (17).

$$\hat{p} = \hat{A}_{corr\ avg}\left(e^{ikx} + \hat{R}e^{-ikx}\right) \tag{16}$$

and

$$\hat{u} = \frac{1}{Z_0}\hat{A}_{corr\,avg}\left(e^{ikx} - \hat{R}e^{-ikx}\right) \tag{17}$$

Assuming the frequency and $\left|\hat{R}\right|$ is known, $\hat{A}_{corr}$ was obtained from $\hat{p}_{i,\mathrm{corr}}$ using

$$\hat{A}_{corr} = \frac{\hat{p}_{i,corr}}{\left(e^{ikL_i} + \hat{R}e^{-ikL_i}\right)} \tag{18}$$

This complex pressure amplitude is constant throughout the impedance tube. The error in the complex amplitude $\hat{A}_{corr}$, calculated using pressure histories from each DPT, was less than 1%. The repeatability of these data was very good with the standard deviation in $\hat{A}_{corr}$ for five tests using each DPT was 0.063, 0.061, and 0.064, respectively. The average $\hat{A}_{corr}$ was used in the calculation of the acoustic pressure and velocity distributions.

5.3 Isolation of the Area-Contraction Calculation of impedance.

To obtain the acoustic response solely due to the area-contraction, two sensors were placed upstream on the sense-line using the TMBs previously described. These TMBs were clamped directly to the sense-line at predetermined distances from the sample location. These distances

were determined using the sensitivity analysis previously mentioned. Since data was only taken at one frequency corresponding to the phase flip of the quarter wave resonance of the sense-line, only two sensors were needed upstream of the area-contraction. The same data reduction process was applied to these data obtaining the reflection coefficient, dimensionless impedance, acoustic pressure and velocity amplitude at the area-contraction. The dimensionless impedance for the upstream data can then be subtracted from the corresponding impedance tube data using

$$\hat{\zeta}_{AC} = \left(\frac{\hat{\zeta}_{IT}}{S_{IT}} - \frac{\hat{\zeta}_{SL}}{S_{SL}} \right) S_{IT} \tag{19}$$

where S_{SL} is the cross-sectional area of the sense-line, and S_{IT} is the cross-sectional area of the impedance tube.

The following section presents an analytical sensitivity analysis that has been validated with experimental results to obtain the optimal sensor spacings and distances for the three DPTs used in this study.

5.4 DPT Confirmation Experiments and Sensitivity Study

The tests and analytical results described in this section were conducted to experimentally determine the best possible DPT spacing and distances from the sample location of the impedance tube used in this study. In addition, the accuracy of the reflection coefficient obtained using the developed impedance tube was estimated with the sensitivity analysis, derived by Scarborough[25], in conjunction with experimental data.

In the two-microphone method, and subsequent multiple-microphone method, Boden and Abom[53] found that a longer sensor spacing was better for measuring low frequencies and shorter sensor spacings are better for measuring high frequencies. The reason for this is as follows. Measurement error and random error, or signal to noise error, can be minimized by maintaining that sensor spacing is as close as possible to the driving wavelength. This implies that the sensor spacing should be small for short wavelengths and long for long wavelengths. A short sensor spacing will reduce the accuracy of measurements at low frequencies because the difference of the measurements taken on the standing pressure wave approaches unity when the wavelength of that frequency is much greater than the sensor spacing itself. Likewise, if the difference between the pressure measurements is small, then it is likely that this difference is on the same order as random errors or noise causing a decrease in signal to noise ratio. It was also found in the literature that the reference microphone in the multiple-microphone method must be at least one duct diameter away from the sample location to avoid the effects of near fields and noise. [53] Both DPT spacing as well as distance from the sample location must be considered in order to obtain the high-accuracy low-error measurements desired in this study. Thus, a sensitivity analysis was used in conjunction with experimental measurements to find the total error associated with measuring the complex reflection coefficient.

Scarborough[25] took the total derivative of the complex reflection coefficient equation shown in Eq. (5) with respect to the pressure ratio $P_R = \frac{\left| \hat{p}_{1,corr} \right|}{\left| \hat{p}_{i,corr} \right|}$ to obtain Eq. (20).

$$\frac{d\hat{R}}{dP_R} = \left[\frac{-e^{ikL_2}}{P_R\, e^{-ikL_2} - e^{-ikL_1}} - \frac{\left(e^{ikL_1} - P_R\, e^{ikL_2}\right)\left(e^{-ikL_2}\right)}{\left(P_R\, e^{-ikL_2} - e^{-ikL_1}\right)^2} \right]. \tag{20}$$

Measurement error of 1% was assumed and multiplied by Eq. (20) to obtain the total error due to measurement of the pressure ratio yielding

$$\hat{E}_R = \frac{d\hat{R}}{dP_R}\delta P_R \tag{21}$$

where δP_R is the assumed error in the measurement of the pressure ratio and $\hat{E}_R$ is the total error in the complex reflection coefficient.

The sensitivity analysis presented above, allows the user to input theoretical distances from the sample location assuming a pressure ratio that yields $\left|\hat{R}\right| = 1$ and $\varphi\left(\hat{R}\right) = 0$ for all frequencies of interest. As previously mentioned, the minimum and maximum possible DPT spacing for the impedance tube used in this study was found to be $\geq 50\ mm$ and $\leq 203.2\ mm$, respectively. These DPT spacings were input into Eq. (21) to determine which frequencies present high measurement error above 1%. The ideal cutoff, approximately half the indeterminate frequency for a given DPT spacing, was also determined for the data stitching process previously described. Starting with the minimum and maximum DPT spacings above, the magnitude of the total error $\left|\hat{E}_R\right|$ for several permutations of DPT spacings and distances from the sample location were calculated for the frequency range of interest previously described. The set of SPT spacings with the lowest measurement error across the frequency range of interest was chosen to be the optimal DPT spacing for both low frequency data and high frequency data. These analytical calculations indicated that the best possible minimum and

maximum DPT spacing was 50.8 mm and 203.2 mm, respectively. However, since this sensitivity analysis does not account for near field and noise effects close to the sample location, experimental measurements must be obtained to identify the optimal distance from the sample location for the reference DPT and, in general, to validate the sensitivity analysis.

To obtain a wide range of DPT spacing experimental measurements, several DPT ports with known distances from the sample location were installed into the side-wall of the impedance tube described in the beginning of Chapter 4. A 25.4 mm thick rigid aluminum plate was placed at the sample location, simulating a perfectly rigid termination having magnitude and phase of one and zero, respectively. For these experiments, the reflection coefficient was measured for each possible permutation of DPT spacing and distance from the sample location across the frequency range of interest. Each of these test results were reduced using the data reduction process in Chapter 5 and the results for $\left|\hat{R}\right|$ were plotted against. The sensor positions that were closest to $\left|\hat{R}\right| = 1$ and $\varphi\left(\hat{R}\right) = 0$, were considered optimal. The optimal position for each DPT from the sample location was determined to be 76.2, 127, and 279.4 mm for the reference DPT, DPT two, and DPT three, respectively. Measured data using the optimal DPT distances can now be compared to the analytical calculations, that used the same distances, to validate the sensitivity analysis.

During this investigation, it was found using the sensitivity analysis that three sensors would be enough to obtain high-accuracy acoustic response data across the frequency range of interest. For brevity, a single case of measured data and calculated total error, using the optimal DPT spacings previously mentioned, are compared to determine how well the sensitivity analysis predicts measurement error in high-error frequency ranges. Figure 16 shows low frequency data and the total error in measuring the pressure ratio using the minimum DPT spacing of 76.2 mm and 127 mm from the sample location. These data indicate high measurement error due to low signal to noise ratios at frequencies $\leq 270\ Hz$ and an error of $\geq 6\%$ in $\left|\hat{R}\right|$ for this DPT spacing. As frequency decreases, the total error increases in the sensitivity analysis. This is also the case for measured data below 270 Hz.

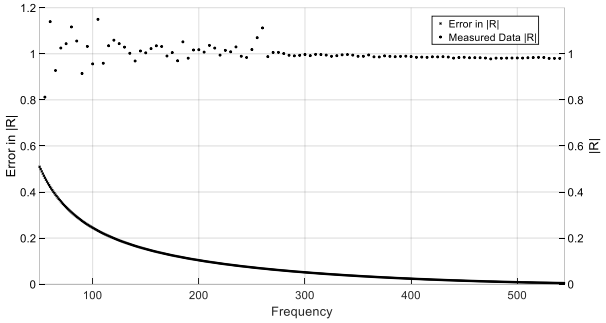

Figure 16: Measurement error compared to data taken with a short sensor spacing of 76.2 mm and 127 mm from a rigid end termination.

Figure 17 shows experimental data across the entire frequency range of interest for the maximum DPT spacing of 76.2 mm and 279.4 mm. Measurement error asymptotically increases at a central frequency of approximately 845 Hz. The measured data also agrees with the calculated total error at this frequency, thus validating the accuracy of the sensitivity analysis. Referring to Chapter 4, the calculation of the indeterminate frequency for

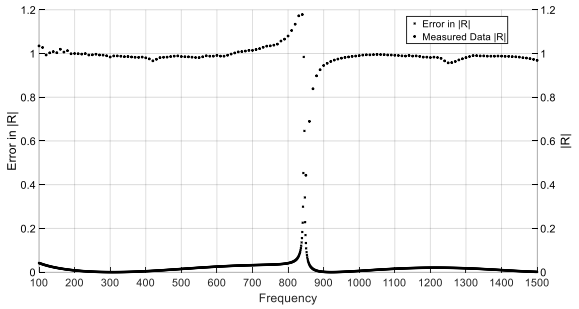

Figure 17: Measurement error compared to data taken with a long sensor spacing of 76.2 mm and 279.4 mm from a rigid end termination.

this DPT spacing yields a similar result of 844 Hz. As the driving frequency approaches this indeterminate frequency, naturally the error in measuring the pressure ratio will increase to 100%. As frequency decreases from 845 Hz, the total error decreases until reaching a measurement error of $\leq 700\ Hz$ in the $\left|\hat{R}\right|$. Measurement error begins to decrease as frequency increases from 845 Hz. This is most likely due to the DPT measuring the pressure on the downward sloping side of the following peak of the standing wave. These data were determined to have a low order of confidence in experimental testing due to spontaneous and error prone features forming in this frequency range. An example of this phenomenon is shown at approximately 1250 Hz. During data repeatability studies, these features were shown to be unrepeatable.

The sensitivity analysis in conjunction with experimental measurements yielded the optimal DPT spacing and distances from the sample location with high accuracy in the measurement of $\left|\hat{R}\right|$. Simultaneously, the experimental measurements validated the sensitivity analysis. Based upon the calculated error associated with measuring the pressure ratio, the

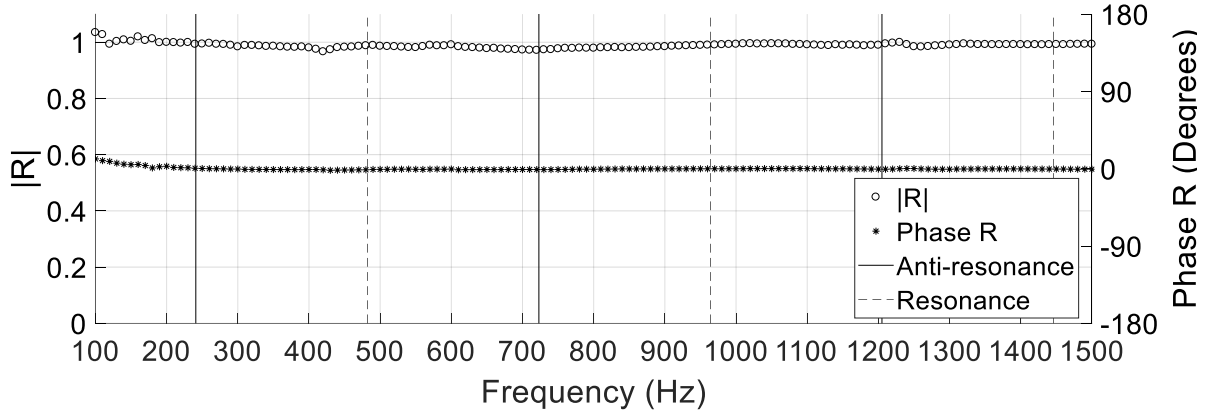

Figure 18. (a) Magnitude of the reflection coefficient and (b) phase of the reflection coefficient as a function of frequency for a closed – closed impedance tube for validation.

longest DPT spacing was determined to be effective for frequencies between 100 Hz and 450 Hz, while the shortest DPT spacing was determined to be effective for the frequency range of 450 Hz up to 1500 Hz.

Figure 18 shows results for the magnitude and phase of the reflection coefficient as a function of frequency using the optimal DPT spacing discussed above. Over the range of frequencies tested, the magnitude of the reflection coefficient was nearly constant with an average value of 0.989 with a standard deviation of 0.009. The average reflection coefficient phase and standard deviation was 1.21 degrees and 0.003, respectively.

It is shown in Figure 18 centered at 430 Hz, there is a slight dip in the magnitude of the reflection coefficient. This feature corresponds closely to the calculated half-wave resonance of the impedance tube calculated to be 482 Hz. A slight rise in the magnitude of the reflection coefficient is also at about 1225 Hz. This rise corresponds very closely to the calculated 5/4 wave anti-resonance of the impedance tube. The data at frequencies below 200 Hz in the magnitude and phase shows increased error and deviation from the mean. This is due to low signal to noise ratios causing an increase in measurement error.

The following section discusses data repeatability for each test conducted throughout this study. Quantities such as the standard deviation between data sets are also presented to give confidence in the data acquisition process.

5.5 Data Repeatability

This section describes a series of experiments designed to assess the repeatability of reflection coefficient and impedance measurements considering sources of error such as electronic, signal to noise ratio, and human error. Previously described frequency and amplitude

varying tests were conducted in sets of three for the determination of data repeatability. The standard deviation and mean was calculated for each set of three tests. For brevity, a single calculation of the standard deviation for a typical set of frequency-varied data and amplitude-varied data was found to be 0.0841 and 0.0834 respectively. This was then confirmed by repeating the process, calculating the standard deviation of both the magnitude of the reflection coefficient and real part of the impedance for a calibration, validation, sense-line, and amplitude-varied test all yielding a standard deviation comparable to that of 0.083 to 0.084. This standard deviation in the magnitude of the reflection coefficient and real part of the impedance is sufficiently low to determine that the data is highly repeatable and an in-depth analysis of the repeatability of further tests was deemed unnecessary.

The following chapter presents the results obtained with the impedance tube described in Chapter 4. Two overarching studies were conducted to characterize the longitudinal nonlinear acoustic response of (a) four sense-lines with different inner diameters subjected to no flow conditions and (b) a single sense-line geometry with varying flow conditions.

Chapter 6

Results and discussion

In this chapter, a sense-line was simulated by attaching extension-tubes with different length to diameter ratios to the sample location of the impedance tube previously described. Two studies were conducted to investigate various effects. For the first study, the acoustic response of differing extension tube inner diameters without purge air flow was investigated. For the second study, the application of purge air flow in a single sense-line geometry was investigated.

6.1 A Study on Varying Area-Ratio Sense-Lines

The acoustic response of four 203.7 mm long, rigidly terminated extension-tubes, with varying area-ratios were of interest. The area-ratio is defined as $\sigma = A_{IT} / A_{SL}$ or the cross-sectional area of the impedance tube divided by the correctional area of the sense-line. The four extension-tubes used in this study had inner diameters of 4.57, 10.92, 17.27, and 23.62 mm with corresponding area-ratios of 122.8, 21.5, 8.6, and 4.6, respectively. The sections below present results of frequency response and amplitude response experiments for each of these extension-tubes.

The following sections present experimental results of experiments to determine (1) the normalized damping and power absorption on frequency, (2) the acoustic end correction, (3) the nonlinear acoustic impedance of (a) the sense-line, (b) the extension-tube, and (c) the area-contraction for each of the extension-tubes described above. Each experiment was conducted at atmospheric temperature and pressure and was not subjected to steady mean flow.

6.1.1 Frequency Response of Different Area-Ratio Extension-Tubes

This section presents measurements of the reflection coefficient, acoustic power absorption coefficient, and impedance of sense lines for a range of frequencies and acoustic pressure amplitudes.

The test procedure for frequency sweep and amplitude sweep experiments is described in section IIB. The reflection coefficient and impedance were obtained from these experimental data as described in sections II-C through II-F. The normalized power absorbed by the sense-line was obtained from experimentally measured reflection coefficients using

$$\alpha = \left(1 - R \cdot R^{*}\right) = \frac{2}{\frac{\left(|\zeta|^{2}+1\right)^{2}}{\mathrm{Re}(\zeta)} - \mathrm{Re}(\zeta)} \tag{22}$$

Figure 19 shows plots of the magnitude and phase of $\hat{R}$, α, $\left|\hat{P}\right|$, and $\left|\hat{V}\right|$ as a function of frequency. Figure 14(a) shows that $\left|\hat{R}\right|$ is less than unity for a narrow band of frequencies centered at approximately 410 Hz and 1235 Hz for each extension-tube indicating acoustic damping is present.

Figure 19(d) shows that for $\sigma = 122.8$ at 410 Hz the acoustic velocity magnitude is nearly zero and $\left|\hat{R}\right| = 0.79$ which corresponds to 37.6% of the incident sound energy being dissipated. As the area-ratio decreases, energy dissipation increases to its maximum value at an area-ratio of 21.5. For area-ratios below 21.5, $\left|\hat{R}\right|$ increases due to reduced energy absorption by the area-contraction. For $\sigma \to 1$, $\left|\hat{R}\right| \to 1$ and $\alpha \to 0.$ Therefore, for large area-ratios, the area-contraction and extension tube together tend to respond increasingly like a rigid termination.

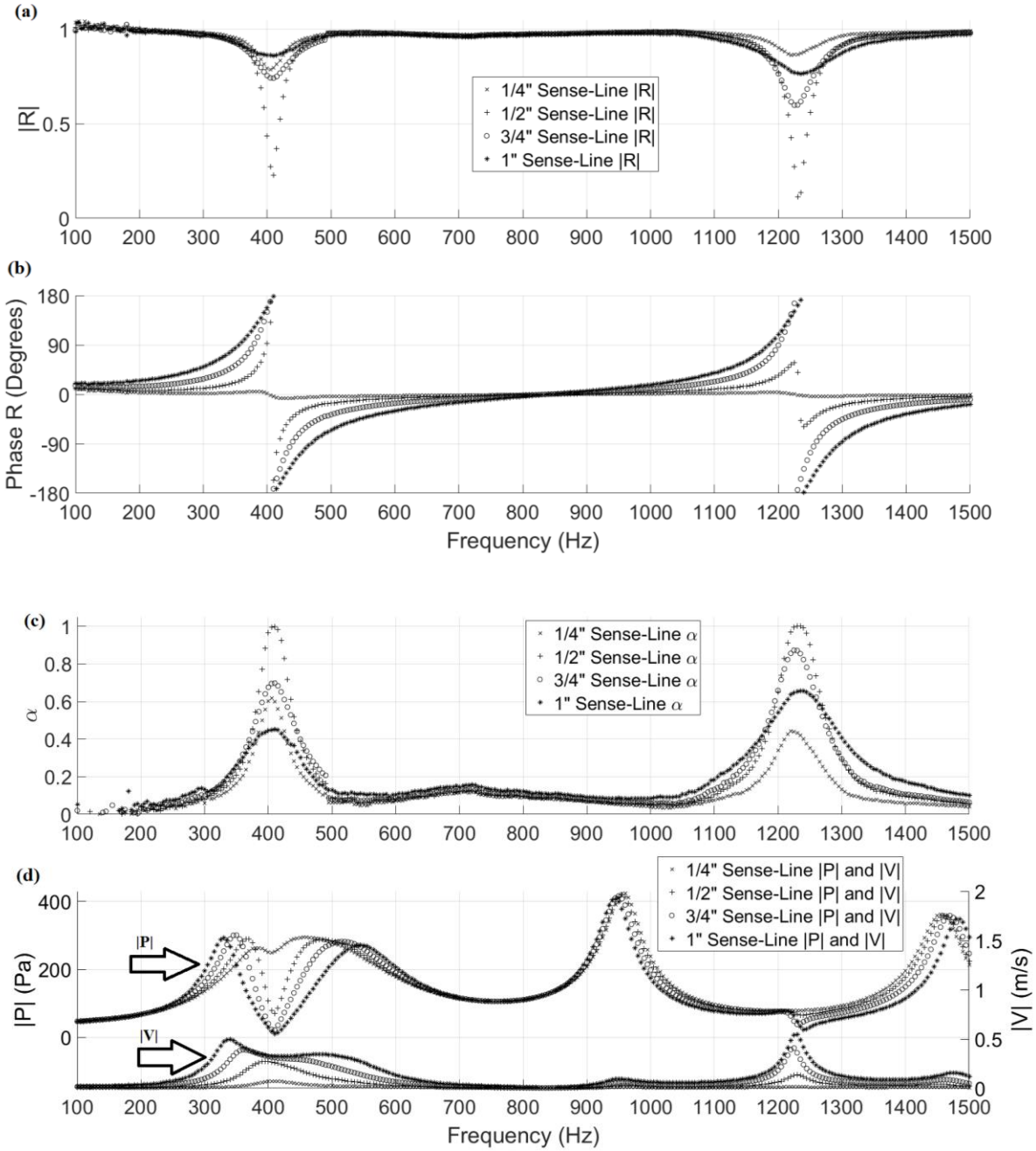

Figure 19: From top to bottom, (a) The magnitude of the reflection coefficient, (b) phase of the reflection coefficient, (c) acoustic power absorption coefficient, (d) and the magnitude of the acoustic velocity and acoustic pressure as a function of frequency for the (a) 5.08, (b) 10.44, (c) 16.89, and (d) 23.22 mm diameter sense-lines.

Eq. (22) indicates that the power absorbed is zero for very large $\mathrm{Re}(\zeta)$ or $\mathrm{Re}(\zeta) \to 0$ for all $\mathrm{Im}(\zeta)$. The power absorbed is also zero for very large $\mathrm{Im}(\zeta)$ and for all $\mathrm{Re}(\zeta)$.

Figure 19(d) shows that the acoustic velocity amplitude increases as $\sigma \to 1$ at the frequency of maximum damping (410 Hz). The velocity for $\sigma = 4.6$ exhibits some interesting characteristics. The maximum velocities do not coincide with the resonant frequency of the extension-tube, 410 Hz. Instead, the highest acoustic velocities appear at 340 Hz and 1230 Hz, respectively. Based on the available data it is hypothesized that as $\sigma \to 1$ these acoustic velocity maxima will continue to shift away from the ¼ wave extension-tube resonance and toward the half and full-wave system resonances of 307 Hz and 614 Hz, respectively, computed for $\sigma \to 1$. There are also velocity maxima located at 940 Hz, 1230 Hz, and 1480 Hz corresponding to the 921 Hz, 1227 Hz, and 1535 Hz half wave system resonances, respectively. The velocity maximum at 1230 Hz corresponds to the combined effects of the ¾ wave resonance of the extension-tube and the 4/2 wave resonance of the system.

The phase of the reflection coefficient for each extension-tube is shown in Figure 19(b)**.** It is shown that the phase is constant except near the resonant frequencies of each extension-tube. Each frequency at which the reflection coefficient phase changes sign is precisely one of the extension-tube resonances. These frequencies for the ¼ wave resonance of the extension-tube are 405, 410, 405, and 410 Hz for the 5.08, 10.44, 16.89, and 23.22 mm inner diameter extension-tube, respectively, as measured using a frequency resolution of 5 Hz increments. For the ¾ wave extension-tube resonant frequencies were measured to be 1230, 1235, 1230, and 1235 Hz for 5.08, 10.44, 16.89, and 23.22 mm diameter extension-tubes, respectively.

Figure 20 shows a plot of the magnitude and phase of the reflection coefficient for a 402.6 mm long extension-tube with $\sigma = 1$. This plot demonstrates that for an area-ratio of one, the phase roll-offs, or the locations at which the phase changes sign, are perfectly diagonal across the entire frequency range having a slope of 0.0147. This confirms the previous assertion that as $\sigma \to 1$, the phase of the reflection coefficient trends closer to a diagonal line. The extension-tube length, or rather the distance from the measurement location to the rigid end termination, can be

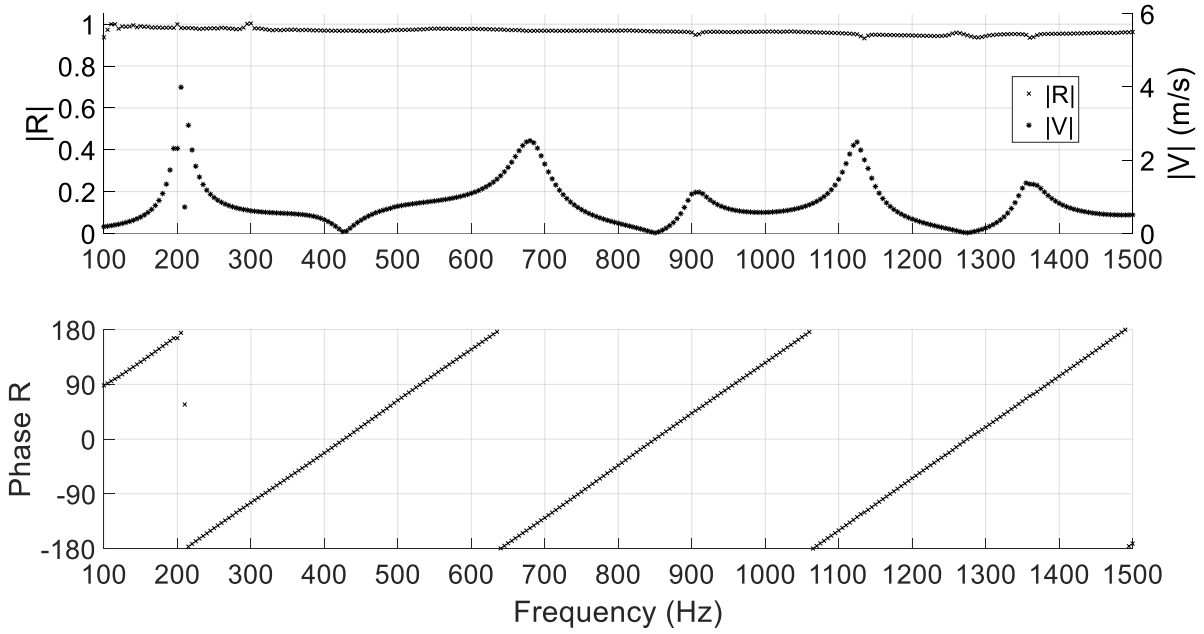

Figure 20. Magnitude and phase of the reflection coefficient for a 402.6 mm long extension-tube illustrating the acoustic response of an area-ratio equal to 1.

obtained from the slope of the phase roll-offs by $L_{eff} = \frac{\left(\frac{d\phi}{df}\right)c}{4\pi}$, where $\frac{d\phi}{df} = \frac{\phi_2 - \phi_1}{f_2 - f_1}$ yielding a length of 401.8 mm. This length compares within an error of 0.2% of the geometric length which is 402.6 mm. Each phase sign change corresponds to a resonant frequency of the 402.6 mm long extension-tube. The magnitude of the reflection coefficient, on average, has a slight negative

slope and is, excluding a few outliers, constant. The magnitude of $\hat{R}$ shows that as $\sigma \to 1,$ the net damping due to the extension-tube goes up. This damping in Figure 20 steadily increases as the frequency increases and, using Eq. (22) has an acoustic power absorption of 4% to about 9% at 200 Hz and 1400 Hz, respectively.

The next section presents measurements of the real part of the impedance as a function of acoustic velocity amplitude $\left|\hat{V}\right|$. The impedance measurements in the following sections were obtained using the same driving frequency specific to each σ, DPT spacing and distance from the area-contraction, and DSW range.

6.1.2 Sense-Line Impedance

This section describes experimental measurements of extension tube acoustic impedance. In particular, the study focused on how the real part of the acoustic impedance, i.e., resistance, depends on the magnitude of the acoustic velocity $\left|\hat{V}\right|$. For these studies, the driving frequency was set to the ¼ wave resonance of the studied extension-tube, which also corresponds to the frequency of maximum damping, and the driving amplitude was varied from near zero to the maximum attainable amplitude.

Figure 21 shows a plot of the extension tube resistance vs. acoustic velocity amplitude. These data reflect the net acoustic response of the combined area-contraction and extension-tube. These data show that the resistance of the extension tube depends on acoustic velocity amplitude, i.e., it is nonlinear. The following three distinct regions shown in the measured data were identified: (1) a constant-slope high-amplitude region, a transitional region, and an acoustic velocity amplitude independent region. These regions are readily apparent the $\sigma = 122.8$ case.

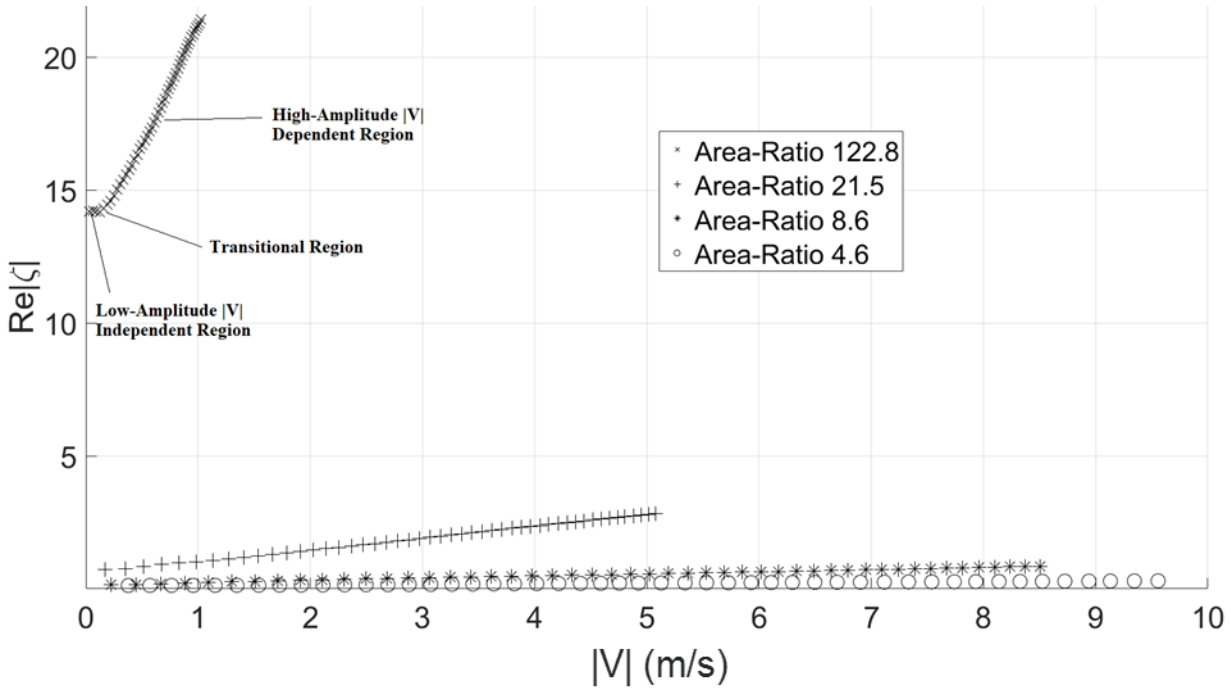

Figure 21: The measured acoustic resistance as a function of the acoustic velocity amplitude at the ¼ wave mode frequency for extension-tubes with area-ratios of 4.6, 8.6, 21.53, and 122.84.

For this case, there is a region of constant resistance below $\left|\hat{V}\right| = 0.06\ \frac{m}{s}$ beyond which the resistance transitions to linear dependence on acoustic velocity amplitude.

These low-amplitude data show that the (linear acoustic) resistance increases with area ratio. The slope of the resistance also increases with increasing area ratio. Due to the reduced resistance, the maximum acoustic velocity amplitude that could be driven using the setup described above increases with decreasing area ratio.

Figure 22 shows a more detailed plot of low-amplitude data indicating that the resistance does not depend on acoustic velocity amplitude for these amplitudes, i.e., these data indicate a linear acoustic response. To maximize signal to noise ratio and limit measurement error to less than 5%, the lower driving limit for this study was $0.05\ \frac{m}{s}$, which corresponded to a SPL of 119 dB measured at the area-contraction. The zero driving resistances were found to be 13.901, 0.659, 0.151, and 0.089 for σ was 122.8, 21.5, 8.6, and 4.6, respectively.

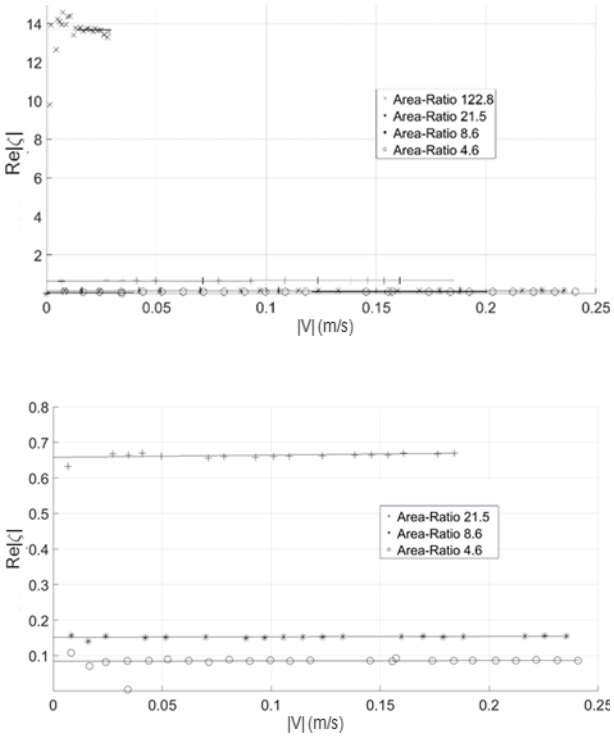

Figure 22: The acoustic resistance as a function of the acoustic velocity amplitude at the ¼ wave resonance of each extension-tube in this study at the low-amplitude driving range. (a) view of all four area-ratio extension-tubes, (b) view of the lowest three area-ratios.

6.1.3 Extension-Tube Impedance

Acoustic response measurements were also obtained in each extension-tube using the multiple microphone method by mounting dynamic pressure transducers along the length of the extension tube as described above.

Figure 23 shows the extension tube resistance as a function of acoustic velocity amplitude as measured in each extension-tube. The measured resistances described here are likely due to extension-tube wall viscous and thermal damping.[82, 83] However, this was not confirmed as it was not the focus of the study.

These data show that the acoustic resistance for each extension tube is quite small compared with the corresponding acoustic resistance shown in Figure 22. The resistances for $\sigma = 21.53,\ 8.61,$ and 4.6 appear to all cluster very close to each other between 0.018 and 0.028. These data all appear to have a small, on average, negative slope. However, when scaled to the same resistances presented in Figure 21, these data are independent of acoustic velocity amplitude. Based on these data, we expect the resistances to go to zero as $\sigma \to 1.$ Data for the

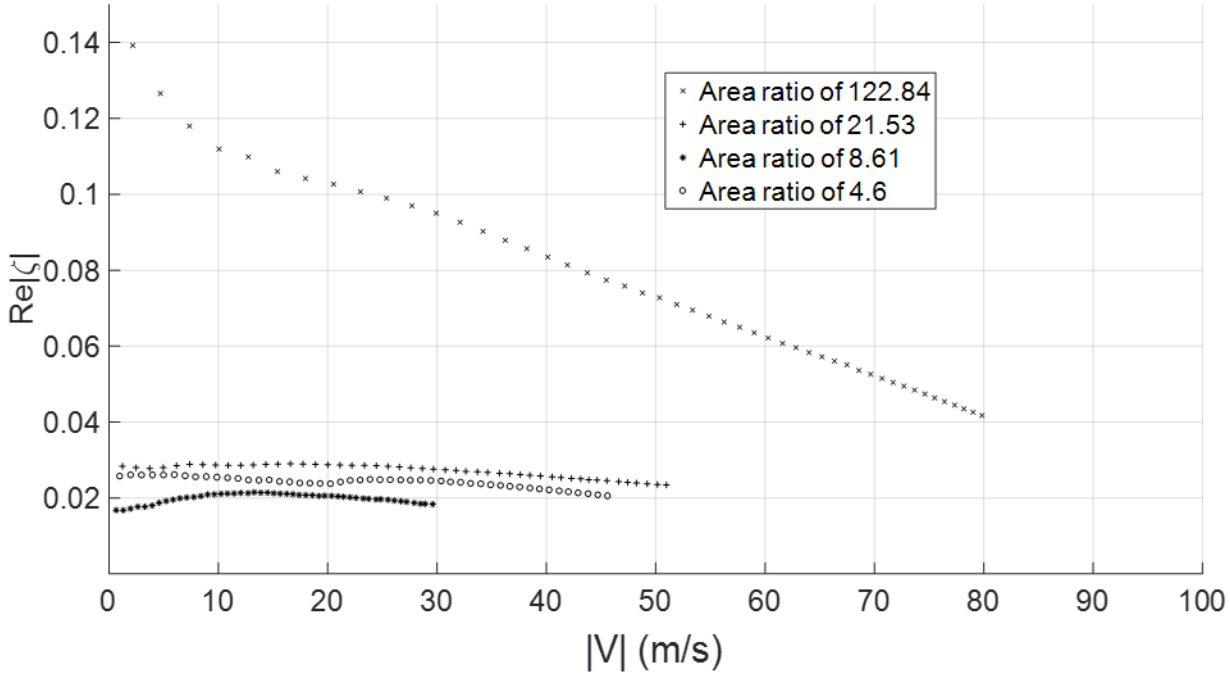

Figure 23. Resistance as a function of acoustic velocity amplitude as taken in each extension-tube.

case where $\sigma = 122.84$ appears to have a dependence on $\left|\hat{V}\right|$ with a constant negative slope above approximately $\left|\hat{V}\right| = 30\ \frac{m}{s}$.

It is important to point out that the measured resistance for the $\sigma = 8.61$ case was lower than then $\sigma = 4.6$ case when the opposite would be expected. These data are on average within a dimensionless resistance of 0.002 of each other and are slightly under the confidence interval of repeatability. Repeatability tests revealed that these data had a standard deviation of 0.0024 for $\sigma = 4.6$ and 0.0023 for $\sigma = 8.61$. When converted to the acoustic resistance rather than the dimensionless resistance, which scales based on the inner diameter of the extension-tube, these data will align in the expected order. Furthermore, this expected ordering is confirmed by measuring the impedance of an extension tube with an $\sigma = 1$ yielding resistances of zero across all $\left|\hat{V}\right|$.

6.1.4 The Acoustic End-Correction

This section presents extension tube effective length measurements obtained from frequency response experiments. Figure 14(b) shows that the calculated and actual resonant frequencies differ somewhat as σ increases. This phenomenon is attributed to the effective length of the sense-line.[23, 84, 85] These measurements are then compared with the theoretical values for the upper and lower limit of an infinitely-flanged open-closed pipe.

The frequencies at which the $\varphi\left(\hat{R}\right)$ changes sign in Figure 19, closely correspond to the theoretical ¼ and ¾ wave frequencies of the extension-tube. These data show that the measured resonances shift further from the calculated resonances of the extension-tube as σ increases. For an open-closed tube, these frequencies were computed using

$$f_{res} = \frac{(2n-1)c}{4L_{eff}} \tag{23}$$

where $n = 1, 2, 3, \ldots$ and taking the geometric length of the extension-tube as the effective length. The difference between the actual and ideal resonant frequency can be accounted for by adding an end-correction[23] to the geometric length resulting in a reduction in the computed resonant frequency.

The effective length for each extension-tube used in this study, except for the $\sigma = 122.84$ case, was obtained from high-resolution frequency sweep data centered around the ¼ and ¾ wave resonances of the extension-tube as follows. Near the resonant frequencies, the phase of the reflection coefficient abruptly changed sign. The natural frequency was taken to be the frequency at which the phase crossed zero. To improve precision, the zero-crossing frequency, and hence natural frequency, was obtained by interpolating the reflection coefficient phase data. The $\sigma = 122.84$ case was omitted due to high difficulty in obtaining the zero-crossing frequency due to an extremely small phase roll-off. The uncertainty in the zero-crossing frequency yielded unacceptable error in the final results.

High-resolution frequency sweep experiments were repeated three times for each of the three area-ratios considered. The speed of sound was obtained from the average air temperature measured at the area-contraction during each experiment. The average effective lengths L_{eff}, was then calculated at the zero-crossing frequencies. Finally, the average length corrections $L_{corr} = L_{eff} - L_{geo}$ were calculated and normalized by extension-tube radius. These average data are shown in Table I. Also shown are the theoretical upper and lower limits of the end-correction, normalized by tube radius, for an infinitely-flanged tube radiating into an infinite

environment. These are given as $\Delta l = \frac{8r}{3\pi} = 0.85 \, d_{SL}/2$ and $\Delta l = \frac{\pi r}{4} = 0.7854 \, d_{SL}/2$, respectively.[23]

Amplitude dependence of the zero-crossing frequency, and hence, effective length, was investigated by repeating the high-resolution frequency sweep tests for several different driving amplitudes. Despite the observed amplitude dependent damping, the zero-crossing frequencies, and hence effective lengths, were not found to be amplitude dependent.

The calculated end-corrections in *Table **I*** represent the end-corrections for a finite flanged tube in a confined environment. Thus, it is expected that the measured and normalized end-corrections will not correspond to the theoretical values. Furthermore, normalization of these tubes based on diameter may not be suitable for very small tubes as viscous effects become a significant factor. It is also unknown as to what the effect of a confined environment would do to the acoustic response of this flanged tube. Further work will need to be conducted to better understand the end-correction of flanged tubes in the impedance tube used in this study. for each area-ratio lies outside of this theoretical upper and lower limit presented by Blackstock.

Table I. *Average experimental data used in calculating the acoustic end-correction.*

σ	$T\ (K)$	$f_{n=1}\ (Hz)$	$f_{n=3}\ (Hz)$	$L_{eff\ n=1}\ (mm)$	$L_{eff\ n=3}\ (mm)$	$L_{corr\ n=1} * d_{SL}/2$	$L_{corr\ n=3} * d_{SL}/2$
21.53	293.79	406.5	1229.2	210.93	209.27	1.51	1.20
8.61	293.81	410.5	1239.5	208.88	207.54	0.74	0.58
4.6	293.82	412.5	1242.5	207.88	207.04	0.29	0.22

However, these end-corrections are very close to this theoretical range. As $\sigma \to 1$, $L_{corr} \to 0$, which is expected.

6.1.5 Area-Contraction Impedance

This section applies the impedance subtraction process previously described to the sense-line and extension-tube data to obtain the isolated resistance of the area-contraction.

The measured acoustic resistance of the extension tube was removed from the measured resistance of the combined area-contraction and extension tube to obtain the acoustic resistance of the isolated area contraction. The theory and methodology for this subtraction was presented at the end of Chapter 5. This section presents the results for several area contractions. Figure 24 shows the dependence of area contraction acoustic resistance on acoustic velocity amplitude. It is interesting, and reassuring, to note that the zero-amplitude acoustic resistance is approximately

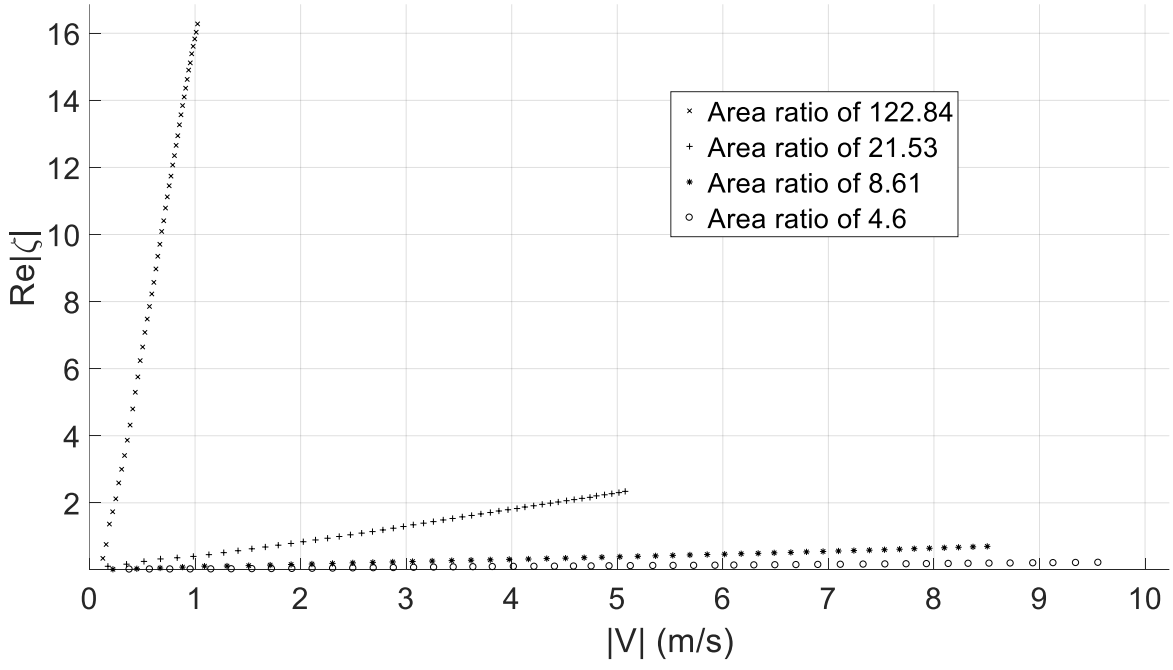

Figure 24. Acoustic resistance as a function of the acoustic velocity amplitude for solely the effects of the area-contraction measured at the ¼ wave resonance of each extension-tube in question.

zero. This indicates that the initial zero-driving resistance was solely due to the thermos-viscous damping along the length of the extension-tube and not due to the area-contraction itself. Comparison of the slope of the data in Figure 21 with Figure 24 shows that the slope decreased slightly after subtracting off the extension tube resistance. This is because the extension-tube data exhibited an on average negative slope for each σ case.

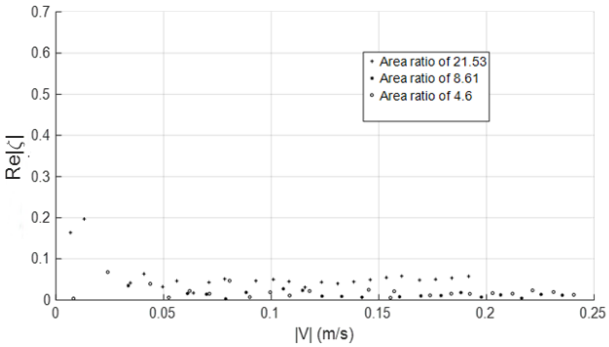

Figure 25. Low amplitude resistance versus acoustic velocity amplitude for the four area ratios in question isolating the effects of the sense-line.

Figure 25 shows the results of impedance subtraction on the low amplitude acoustic response data. The results show near zero resistance for each area-ratio confirming the assertion that the zero-driving resistance is mostly due to extension tube damping. The case with an $\sigma = 122.84$ was omitted due to extremely low signal to noise ratios causing high error in the measurement.

The following section discusses the effects of the broadly known and understood effective length for an infinitely flanged open-closed tube.

6.1.6 Area-Contraction Describing Function and Experimental Data Collapsing

This section presents the measured data from the previous section collapsed with an existing model that describes the nonlinear acoustic response of an area-contraction. This was done to confirm the model's validity.

As described above, theoretically area contraction acoustic resistance scales according to $\left(v_2^2 - v_1^2\right)$. A describing function for the abrupt area-contraction, shown in Eq. (24), was previously derived by Scarborough.[25]

$$Z_{\mathrm{Re}al,i} = \frac{\frac{2}{3\pi}\left|\hat{V}\right|}{c}\left[\left(1+K_{L,i}\right)\sigma^2{}_i - 1\right] \tag{24}$$

Examination of the model reveals that a single loss coefficient, K_L, exists for a given compact area-contraction. The loss coefficient can be thought of as a correction to the geometric area-ratio required to match the experimental data. Otherwise, the model would not fit with the collapsed data. This describing function was used to collapse the measured data as follows.

For each area-ratio, K_L was obtained by first fitting the high-amplitude region data with a line using MATLABs polyfit function. The slope for each line was then computed. The model was set equal to the slope if based on the slope equation $y = mx$, where $x = \left|\hat{V}\right|$ and $y = Z_{\mathrm{Re}al,i}$ yielding

$$Slope_i = \frac{2}{3\pi}\frac{\left[\left(1+K_{L,i}\right)\sigma^2{}_i - 1\right]}{c}. \tag{25}$$

K_L was then solved for. Each area-ratios specific loss coefficient was found to be 0.9485, 0.7052, 0.8641, and 0.7515. The average of these four loss coefficients was 0.8173. This average loss coefficient of $K_L = 0.8173$ was used for each area-ratio. Figure 26 shows that the measured, subtracted, and collapsed high-amplitude region data fits very well with the collapsed model

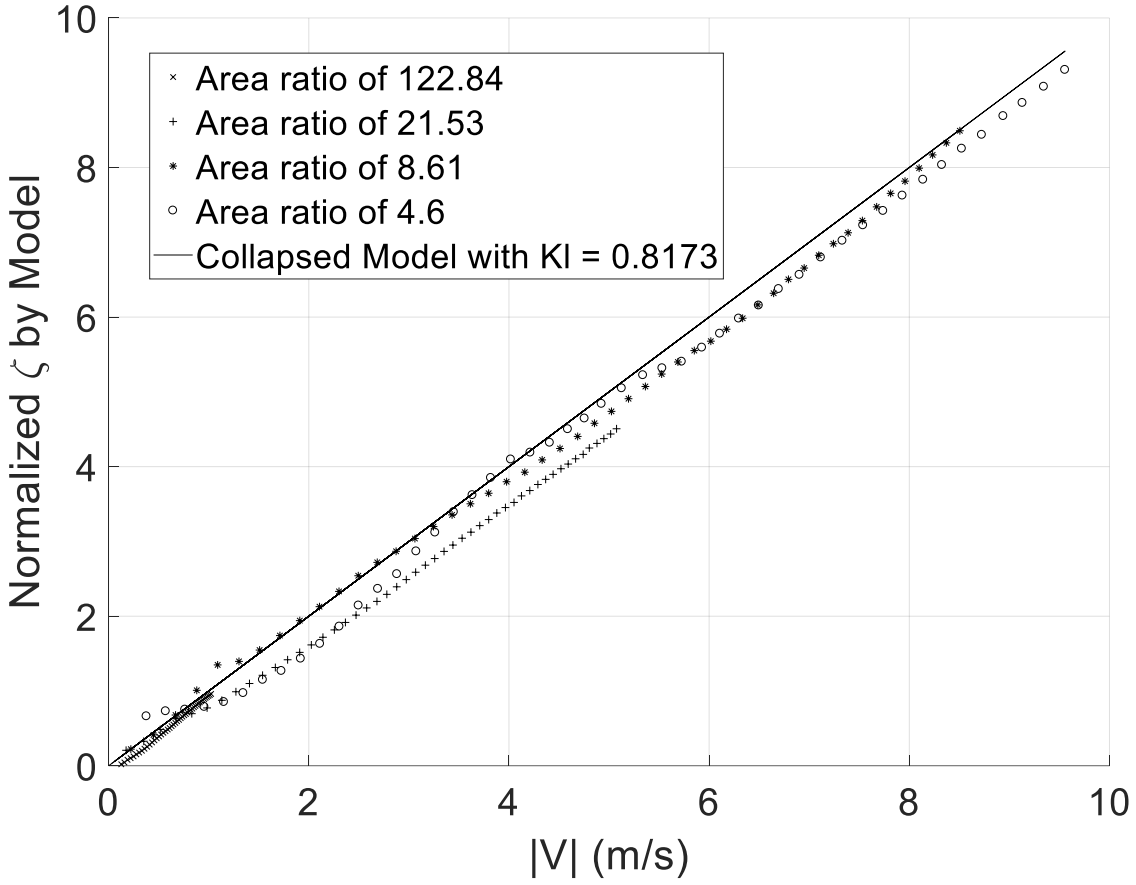

Figure 26. Collapsed acoustic resistance of each area-contraction as a function of the acoustic velocity amplitude measured at the ¼ wave resonance of each extension-tube case with an average $K_L = 0.8173$.

assuming an average loss coefficient of 0.8173.

6.2 A Study on the Acoustic Response of Sense-Lines with Steady Mean Flow

In the following sections, the acoustic response of a single sense-line with a length and inner diameter of 406.4 mm and 10.92 mm, respectively, over a wide range of purge air flow rates, acoustic velocity amplitudes, and frequencies was measured. In addition, purge air flow was applied in both the forward and reverse direction relative to the impedance tube. The multiple-microphone impedance tube used in the previous sections was retrofitted with the flow system described at the end of Chapter 4. The sections below present results of frequency response and amplitude response experiments for several steady mean flow rates applied in the reverse and forward direction of the impedance tube.

The following sections present the results of experiments with the application of steady mean flow to determine the dependence of (1) the normalized damping on frequency, (2) the dimensionless impedance of (a) the sense-line, (b) the extension-tube, and (c) the area-contraction for a single sense-line geometry on acoustic velocity amplitude. Each experiment was conducted at atmospheric temperature and pressure and was subjected to steady mean flow.

6.2.1 Frequency Response of a Single Sense-Line with Flow

This section presents measurements of reflection coefficient and impedance at the ¼ wave resonance of the extension-tube for a single sense-line with steady mean flow, as described in Chapter 4. The reflection coefficient, impedance, and acoustic velocity amplitude were obtained from these experimental data as described in Chapters 4 and 5.

Figure 27 shows a plot of the $\left|\hat{R}\right|$ and $\varphi\left(\hat{R}\right)$ with varying steady flow rates through the sense-line in the reverse direction. As previously discussed, purge air flow in the reverse direction relative to the impedance tube is defined as being applied through the extension-tube and exhausting out the aft end of the speaker mounting block (SMB). At frequencies indicating resonance of the sense-line, as steady mean flow rate increases the magnitude of the reflection coefficient begins to decrease in the magnitude of dampening and starts to broaden in its frequency range. The constant frequencies with minimal damping begin to decrease in the $\left|\hat{R}\right|$ as the steady flow rate increases. The opposite occurs for the magnitude of the acoustic velocity. As the steady flow rate increases, frequency maxima corresponding with resonances of the sense-line begin to increase in acoustic velocity amplitude. The phase of the reflection coefficient acts with the

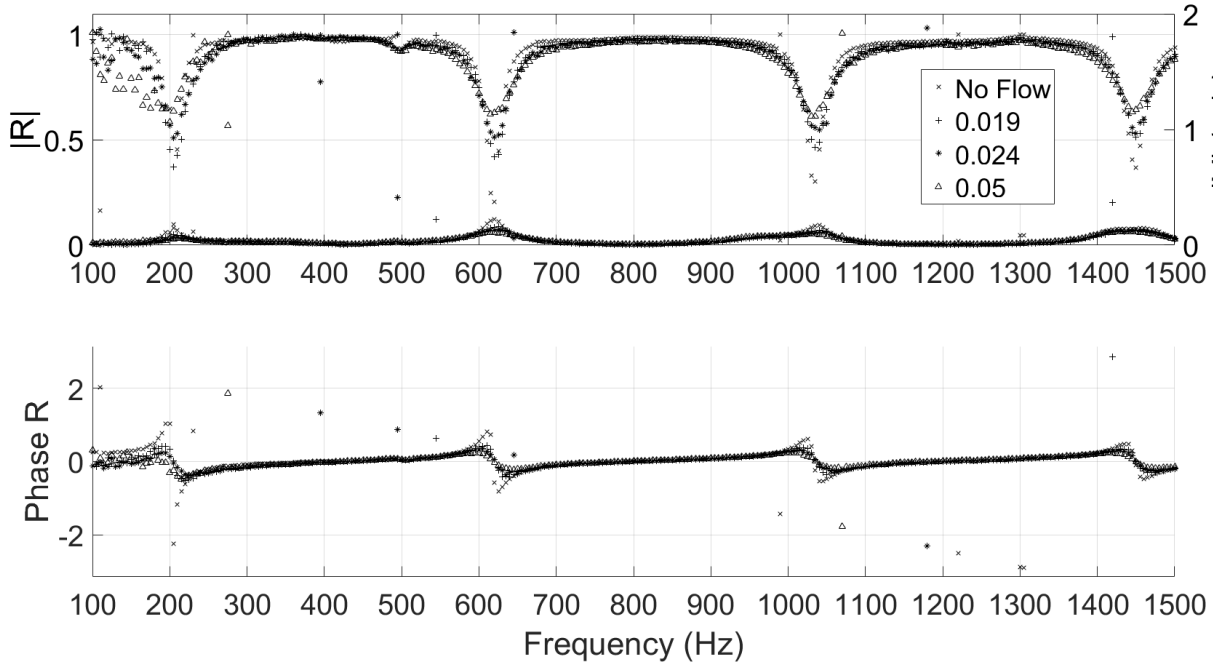

Figure 27. Magnitude of the reflection coefficient and acoustic velocity amplitude versus frequency for a single sense-line length and diameter with varying steady mean flow rates.

magnitude of the reflection coefficient, as the steady flow rate increases the phase roll-offs become less prominent and trend closer to a phase of zero.

The next section presents measurements of the real part of the impedance as a function of $\left|\hat{V}\right|$ with varying steady flow rates in the reverse direction. The impedance measurements in the following sections were obtained using the same ¼ wave resonance driving frequency of the sense-line, DPT spacing and distance from the area-contraction, and driving signal wattage range.

6.2.2 Sense-Line Impedance with Reverse Purge Air Flow

This section presents resistance measurements as a function of $\left|\hat{V}\right|$ for the same sense-line geometry with varying steady flow rates in the reverse direction. As previously described, steady flow is introduced through the sense-line and exhausted to atmosphere at the aft end of the impedance tube. The driving frequency was set at the ¼ wave resonance of the extension-tube, the frequency of maximum damping, and the driving amplitude was varied from near zero to the maximum attainable amplitude by the data acquisition system with a high-resolution amplitude step size.

Figure 28 shows a plot of the acoustic resistance as a function of $\left|\hat{V}\right|$ for varying steady mean flow rates in the sense-line. These data show that the resistance of the control case, the case without flow, has a dependence on acoustic velocity amplitude, or a nonlinear acoustic response. This is to be expected based upon the measurements obtained in the area-ratio study without flow. However, comparing the zero-driving resistances of the data with an area-ratio of 21.54 in the previous study with the data in this study having the same area-ratio yields a discrepancy. Whereas the extension tube with a length of 203.7 mm has an initial zero-driving resistance of 0.659, the data with the same area-ratio in this section for the case without flow has a zero-driving resistance

of approximately one. This discrepancy is expected since it has been shown in the previous study that the length of the extension tube causes the impedance to reflect an initial zero-driving resistance. Since the length of the case without flow in this section is twice the length of the same area-ratio case in the previous study, it is reasonable to see a higher initial driving resistance.

When the steady flow rate is increased, the dependence on $\left|\hat{V}\right|$ begins to decrease. In other words, the slope of these data goes to zero. The dependence of the resistance on $\left|\hat{V}\right|$ disappears at a Mach number of approximately 0.03 in the sense-line. As the Mach number in the sense-line is increased past this steady flow rate, these data appear to remain independent of acoustic velocity amplitude. Similar to the data presented in the previous study on varying area-ratios, each data set in Figure 28 has a zero-driving resistance, or an initial resistance if subjected to no acoustic driving. Based upon previous results, this zero-driving resistance is the product of the resistance due to the

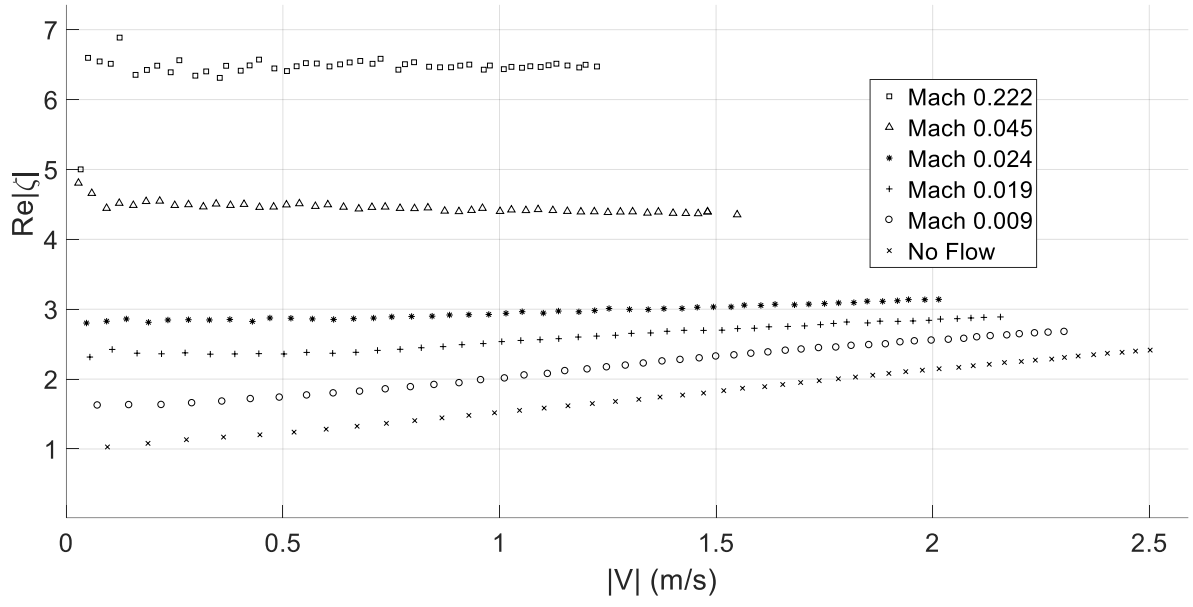

Figure 28. The acoustic resistance versus acoustic velocity amplitude measured at the ¼ wave mode frequency of 205 Hz for varying steady mean flow rates.

length of the sense-line and resistance or driving due to the flow. As the flow rate increases, the initial zero-driving resistance also increases.

Examination of low acoustic velocity amplitude resistances, such as those presented in Figure 22, reveals that noise due to the flow rapidly dominates with even the lowest flow rate. Any trends that would have been present in these data, such as independence of acoustic velocity amplitude, could not be obtained using the current data acquisition system. Data in this region was thus not presented. However, the control case without flow did show an independence of acoustic velocity amplitude with a zero-driving resistance of 0.98. It is hypothesized that if the data with higher flow rates were reached, they would reveal an independence of $\left|\hat{V}\right|$.

The following section discusses measurements of the resistance obtained in the extension tube with varying steady flow rates. This was done to isolate the acoustic response of the area-contraction in a later section.

6.2.3 Extension-Tube Impedance with Reverse Purge Air Flow

This section presents acoustic response measurements obtained in the extension-tube via the use of the TMBs for several steady purge air flow rates. These data will allow for the subsequent isolation of the area-contraction via the impedance subtraction process previously discussed, in the following section.

Figure 30 shows a plot of the resistance as a function of $\left|\hat{V}\right|$ measured in the extension-tube for several steady flow rates. These data indicate an independence of acoustic velocity amplitude for all flow rates shown. The initial zero-driving resistance, or the resistance at which no driving occurs, increases as steady mean flow rate increases. Naturally, as the steady flow rate increases, there is also a decrease in the signal to noise ratio at low $\left|\hat{V}\right|$. This error is shown to be present at low $\left|\hat{V}\right|$ for the steady flow Mach number of 0.222 in the sense-line.

The following section applies the impedance subtraction process to the sense-line and extension-tube data of the single sense-line geometry presented with varying reverse steady purge air flow rates. This subtraction process yields the acoustic response of solely the area-contraction with reverse flow rates.

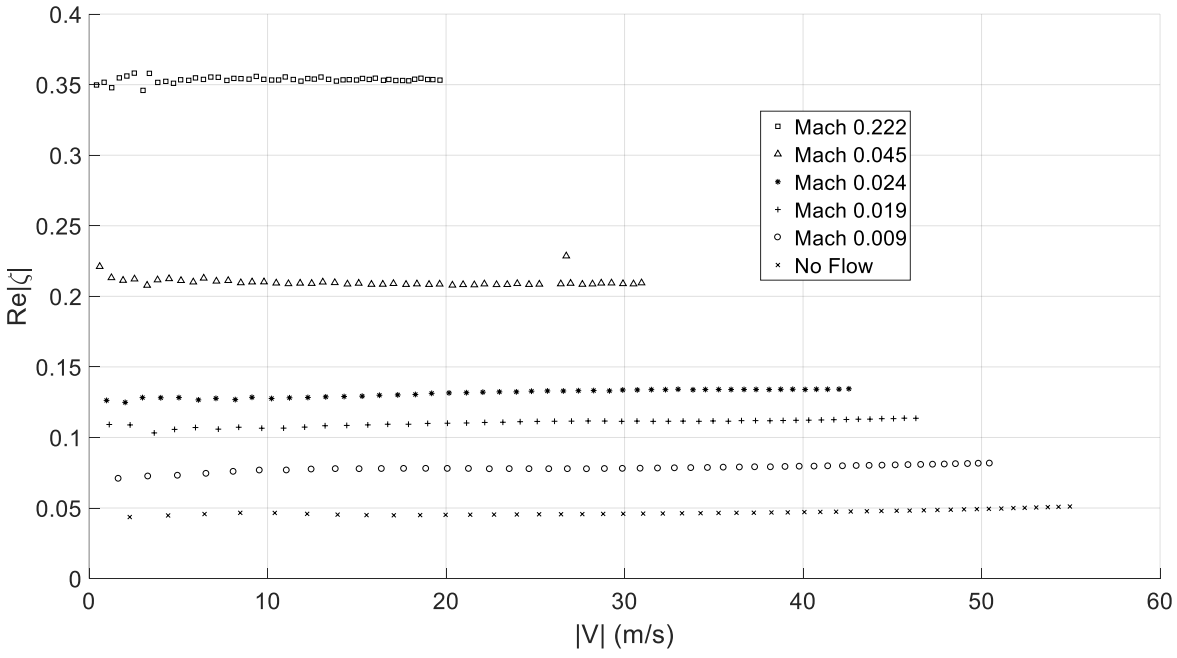

Figure 29. Resistance as a function of acoustic velocity amplitude measured in the extension-tube with varying steady mean flow rates.

6.2.4 Area-Contraction Impedance with Reverse Purge Air Flow

This section applies the impedance subtraction process previously described to the sense-line and extension-tube data presented in the previous sections to obtain the isolated resistance of the area-contraction.

The impedance subtraction process, described in Chapter 5, was applied to the data shown in Figure 28 and Figure 29 to obtain the data presented in Figure 30. These data confirm that the zero-driving resistance is due to the product of the resistance of the sense-line and the resistance or driving due to the flow. Comparing these data to the area-contraction impedance data presented in Figure 24 reveals, again, that the control case without flow is subtracted off to a resistance of approximately zero confirming that the initial zero-driving resistance shown in Figure 28 is solely due to the resistance of the extension-tube. This is also the case for each steady flow Mach number up to approximately Mach 0.03 in the sense-line. Figure 28 shows that when the critical steady flow Mach number is reached in the sense-line the resistance of the system becomes independent of $\left|\hat{V}\right|$. This holds true for data presented after the impedance subtraction process. Beyond this critical Mach number, the resistance of the subtracted data, shown in Figure 31, becomes negative.

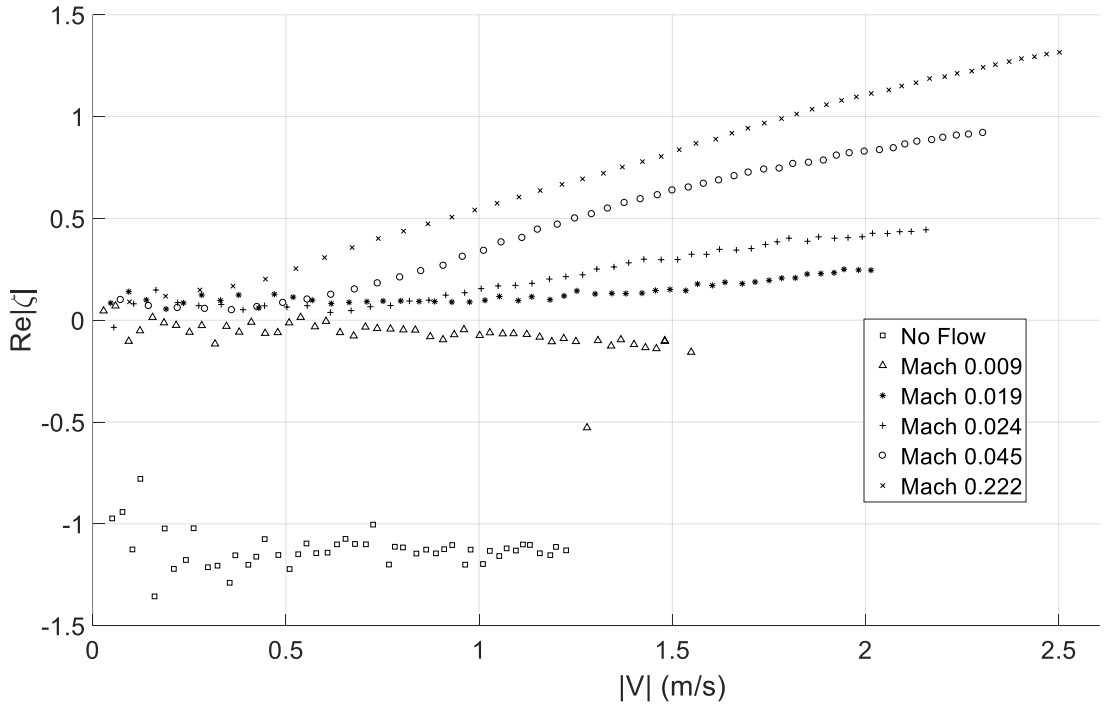

Figure 30. Acoustic resistance versus acoustic velocity amplitude with varying steady mean flow rates in the negative direction relative to the impedance tube with the effects of the area-contraction isolated.

Negative resistances are an indication of driving when the system is subjected to high flow rates in the direction of the reflected wave. This causes energy to be effectively added to the reflected wave. As Mach number is increased, the total energy of the reflected wave increases. This in turn causes the reflection coefficient to increase, which is shown to occur in Figure 27. Thus, the net effect of purge air flow, above Mach 0.03 in the sense-line, in the reverse direction of the impedance tube causes driving in the pressure-history signal. Overall, these data appear to trend in the following manner as the steady flow Mach number increases. The initial zero-driving resistance for cases up to the critical Mach number is zero. As flow increases from there, the data trends to an independence of $\left|\hat{V}\right|$. Once the data is independent of $\left|\hat{V}\right|$, at a steady flow Mach number of approximately 0.03 in the sense-line, the resistance becomes negative indicating driving in the system.

The following section presents measurements of the resistance as a function of $\left|\hat{V}\right|$ with varying steady mean flow rates in the forward direction relative to the impedance tube. The impedance measurements in the following sections were obtained using the same ¼ wave resonant driving frequency of the sense-line used in the previous sections.

6.2.5 Sense-Line Impedance with Forward Purge Air Flow

This section presents resistance measurements as a function of $\left|\hat{V}\right|$ for a single sense-line geometry with varying steady mean flow rates in the forward direction relative to the impedance tube. As previously described, flow is introduced through the aft end of the impedance tube and exhausted to atmosphere at the back of the sense-line. The driving frequency was set at the ¼ wave resonance of the extension-tube, the frequency of maximum damping, and the driving amplitude was varied from near zero to the maximum attainable amplitude by the data acquisition system with a high-resolution step size.

Steady flow is also applied in the forward direction relative to the impedance tube. The acoustic response of sense-lines with reverse as well as forward purge air flow are of interest in this study. Forward steady flow is applied to these experiments by forcing air into the driving end of the impedance tube, traveling through the sense-line, and exiting to atmosphere through the end of the sense-line. Data taken with varying steady mean flow rates in the forward direction of the impedance tube are shown in Figure 31. These data reveal very similar results to those in Figure 28.

The data presented in Figure 31 have an initial zero-driving resistance, which has been shown to be a product of both the resistance of the sense-line and the resistance or driving of the flow in the previous sections. As steady flow increases, the initial zero-driving resistance also increases. Again, as the steady flow rate increases, the dependence on $\left|\hat{V}\right|$ decreases until hitting a critical Mach number. The steady flow Mach number in the sense-line, at which the data becomes independent of $\left|\hat{V}\right|$, is approximately 0.03 calculated at the area-contraction, in the sense-line. This is the same critical Mach number that was found when applying flow in the reverse direction relative to the impedance tube. This indicates that the flow rate at which the data presents independence on $\left|\hat{V}\right|$ is independent of the direction of flow through the sense-line. In examining the data set for the flow case of Mach 0.045 in the sense-line for the forward flow direction, the

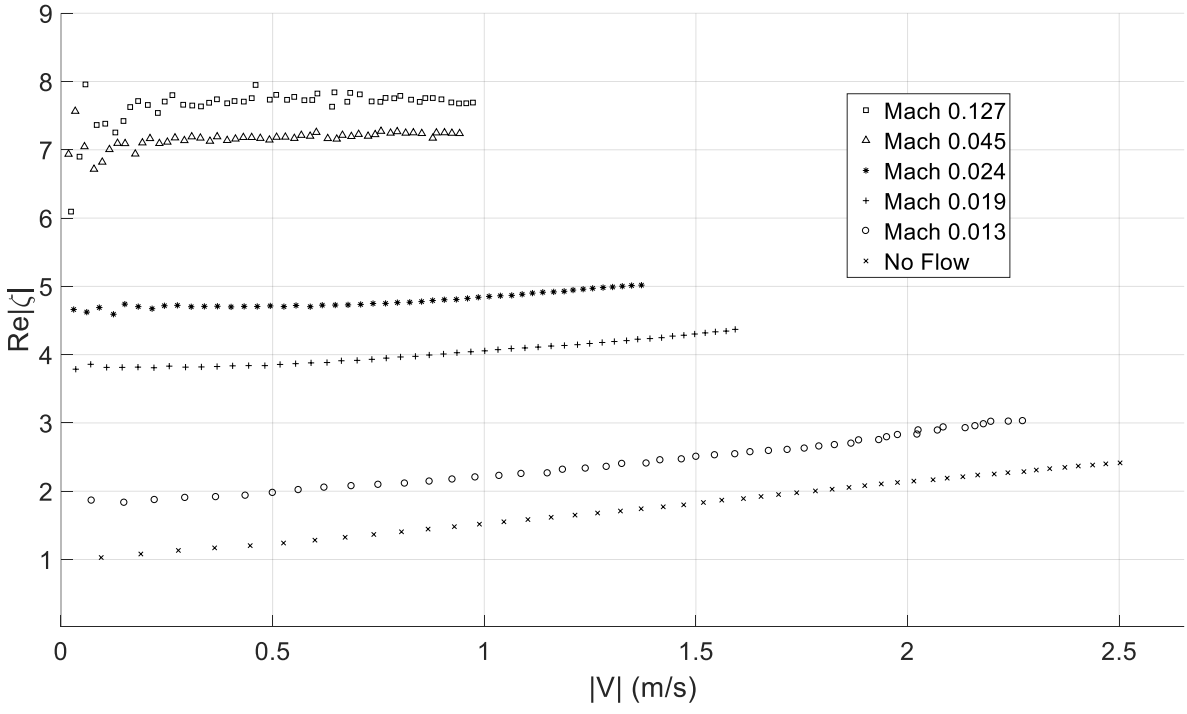

Figure 31. Acoustic resistance versus acoustic velocity amplitude for flow rates applied in the positive direction of the impedance tube.

constant resistance of that flow rate is approximately at a dimensionless resistance of seven. The identical case for the reverse direction is at approximately a dimensionless resistance of 4.5. This indicates that the application of flow in the positive direction increases the resistance of the sense-line.

The following section discusses measurements of the resistance obtained in the extension-tube with varying steady flow rates in the forward direction relative to the impedance tube. These data were obtained to isolate the resistance of the area-contraction in a later section.

6.2.6 Extension-Tube Impedance with Forward Purge Air Flow

This section presents acoustic response measurements obtained in the extension-tube via the use of the TMBs for several steady flow rates in the forward direction. These data will allow for the subsequent isolation of the area-contraction via the impedance subtraction process previously described.

Similar to the data presented in Figure 30, the data shown in Figure 32 indicates an independence of acoustic velocity amplitude for all flow rates shown if scaled to the same resistances presented in Figure 31. The initial zero-driving resistance again increases as steady mean flow rate increases. As steady flow rate increases, there is a decrease in the signal to noise ratio at low $\left|\hat{V}\right|$. This error is present at low $\left|\hat{V}\right|$ for steady flow Mach numbers of 0.222 and

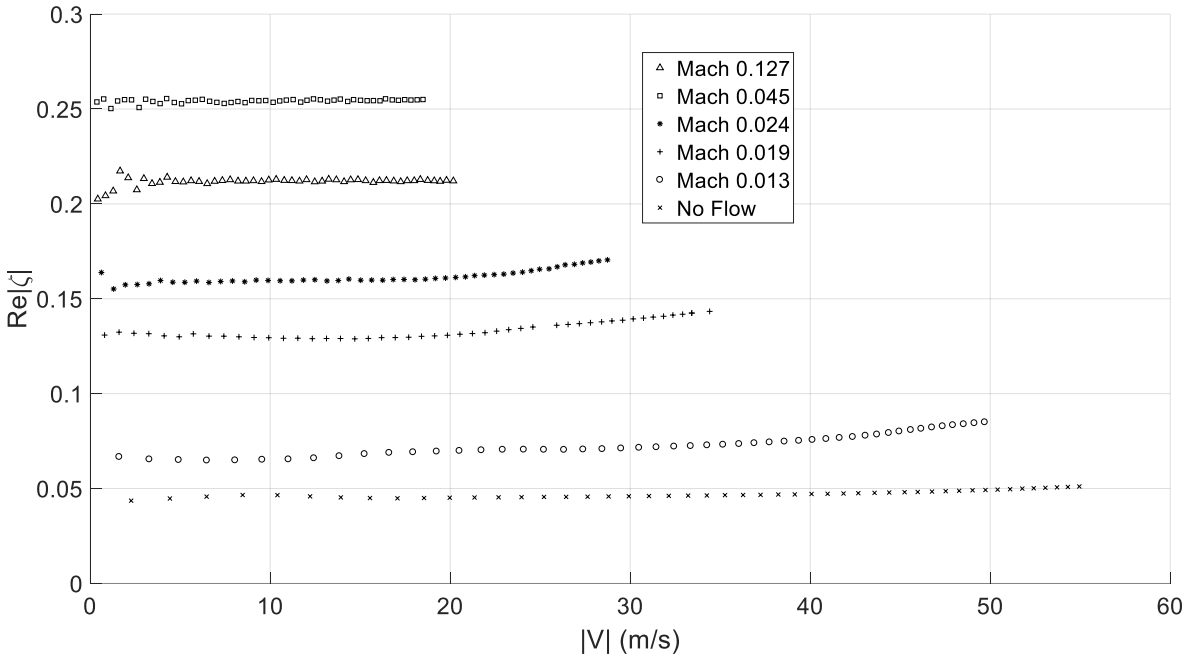

Figure 32. Resistance as a function of acoustic velocity amplitude measured in the extension-tube with varying steady mean flow rates in the forward direction.

0.045 in the sense-line.

The following section applies the impedance subtraction process to the sense-line and extension-tube data of the single sense-line geometry with varying forward steady flow rates. This subtraction process yields the acoustic response of solely the area-contraction with forward flow rates.

6.2.7 Area-Contraction Impedance with Forward Purge Air Flow

This section applies the impedance subtraction process to the sense-line and extension-tube data presented in the previous sections to obtain the isolated resistance of the area-contraction.

Applying the same subtraction process as before, the isolated effects of the area-contraction were obtained for varying flow rates subjected in the forward direction relative to the impedance tube. The data shown in Figure 33, indicates that as steady flow is increased in the forward direction, the resistance of the area-contraction increases. This is due to added energy in the incident wave. As the incident wave increases in amplitude, the ratio of the reflected to incident energies will begin to decrease causing an increase in resistance. The flow case with Mach 0.013

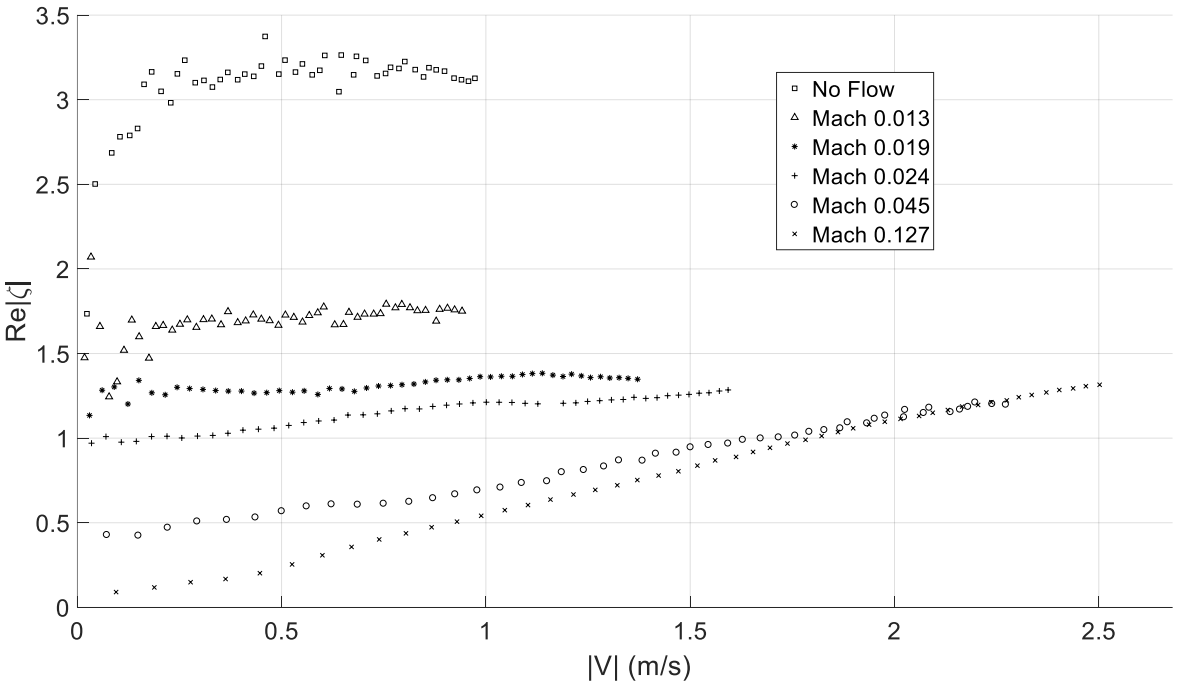

Figure 33. Acoustic resistance versus acoustic velocity amplitude with varying steady mean flow rates in the positive direction relative to the impedance tube with the effects of the area-contraction isolated.

in the sense-line indicates that at an acoustic velocity of 1.8 m/s and up, appears to merge with the data without flow. It could be that each of these data sets are trending towards merging with the control case without flow and this case could be a boundary at which the data cannot cross. On the other hand, these data could be trending towards intersecting with the case without flow and since each data set was driven to the maximum acoustic velocity amplitude possible, this intersection point could have been missed in the data acquisition process. Higher driving capabilities would help to ascertain if these data are trending to merge or to intersect.

The following chapter discusses the conclusions obtained from the data presented in this thesis followed by the future work and questions that remain to be answered.

Chapter 7

Conclusions

This investigation focused on presenting acoustic response measurements of a compact area-contractions and sense-lines under both low and high-amplitude acoustic forcing with and without steady mean flow. These measurements reveal that contrary to linear acoustic theory, the acoustic response of the area-contraction was highly nonlinear when subjected to high-amplitude acoustic forcing without steady mean flow. The isolated acoustic response data of the area-contraction confirmed that the nonlinear effects were indeed caused by the area-contraction and only had a very small effect from the sense-line itself. However, at very low acoustic velocity amplitudes, the nonlinear acoustic response of the compact area-contraction is non-existent. This nonlinear acoustic response was primarily exhibited when the acoustic velocity was high at the open-end of the extension-tube and was due to the area-contraction formed at the connection point of the sense-line to the acoustic-cavity. The acoustic response data of the extension-tube and ultimately of the area-contraction, revealed that the initial zero-driving resistance was solely due to visco-thermal effects in the extension-tube and not due to the area-contraction. The experimental data obtained for four different area-contraction ratios was normalized by a describing function of a compact area-contraction, previously derived by Scarborough.[86] Normalization based on the developed model of the area-contraction acoustic resistance collapsed the data for different area-contraction ratios roughly about a single line. This indicates that the developed model is a useful tool in capturing the dependence of the acoustic resistance on acoustic velocity amplitude. However, it has come to light that these data are

affected by more than just acoustic velocity amplitude. Viscous effects, frequency, and mode shape play a significant role in the acoustic response of area-contractions as well.

Examination of the data with steady mean flow for a single sense-line length and area-ratio revealed that the nonlinear acoustic response of the area-contraction was reduced to a linear acoustic response at low Mach numbers through the sense-line. Observation of the frequency response data revealed that as the steady mean flow rate increased, the damping due to the resonances of the sense-line decreased and the frequencies indicating high dampening due to the resonances began to broaden. The constant regions outside of these frequencies began to exhibit increasing damping as the Mach number in the sense-line increased. It is hypothesized that if the steady mean flow rate continued to increase, the heavy damping regions indicating resonance of the sense-line would "blend" with the constant regions in the magnitude of the reflection coefficient causing constant damping across the entire frequency range of interest. It is estimate based upon the experimental data with steady mean flow that this limiting Mach number in the sense-line is approximately 0.32 and $\left|\hat{R}\right|$ equals approximately 0.8 through the frequency spectra. Further observations of the data reveal that the direction of steady mean flow, relative to the impedance tube, is important to consider. If flow is applied from the sense-line to the impedance tube, the reflected wave will appear to have greater energy than that of the incident wave effectively driving the system as steady mean flow increases. Negative resistances are an indication of driving in the system. The opposite is shown for data with steady mean flow applied from the impedance tube to the sense-line. The incident wave appears to have greater energy than the reflected wave causing the area-contraction resistance to increase as steady mean flow increases.

7.1 Future Work

This work has yielded a better understanding of the nonlinear acoustic response of sense-lines and ultimately area-contractions which ultimately will allow engineers to correct skewed acoustic response data obtained using sense-lines with various purge air flow rates and various area-ratios in unstable combustors. These data have answered several questions pertaining to the nonlinear acoustic response of sense-lines and compact area-contractions. However, there are several other questions to be answered on the topic of acoustically compact area-contractions. One such question yet to be answered is how the area-contractions acoustic response will change with varying sense-line length? Another is how different resonant wave mode frequencies of the sense-line effects the nonlinear acoustic response of the area-contraction? Finally, the literature review suggests that the ultimate goal of this work is to characterize the acoustic response of sense-lines to more realistic engine conditions such as at high pressure, temperature, and eventually reacting flows of liquid and solid propellants. This problem still has a great deal of work to be done in order to fully characterize the nonlinear acoustic response of sense-lines and area-contractions.

Reference Pages

1. Grand View Research, I., *Gas Turbine Market Analysis By Capacity (<200 MW, >200 MW), By Technology (Open Cycle, Combined Cycle), By Application(Power Generation, Industrial, Aviation),Trends & Dynamics, Competitive Landscape, And Segment Forecasts, 2014 - 2025.* Grand View Research, Inc., 2016: p. 130.
2. Foundation, S., *The Space Report 2015: The Authoritative Guide to Global Space Activity.* Space Foundation, 2015: p. 81.
3. Straub, D.L. and G.A. Richards, *Effect of axial swirl vane location on combustion dynamics.* ASME paper, 1999(99-GT): p. 109.
4. Bellucci, V., et al. *On the use of Helmholtz resonators for damping acoustic pulsations in industrial gas turbines*. in *ASME Turbo Expo 2001: Power for Land, Sea, and Air*. 2001. American Society of Mechanical Engineers.
5. Brossard, C., et al. *Effect of swirl injector design and other important parameters on gas turbine combustion*. in *Proceedings of the 36th AIAA/ASME/SAE/ASEE Joint Propulsion Conference, Huntsville, Alabama*. 2000.
6. Culick, F.E. and V. Yang, *Overview of combustion instabilities in liquid-propellant rocket engines.* Liquid Rocket Engine Combustion Instability, 1995. **169**: p. 3-37.
7. Davis Jr, L.B., et al., *Method for staging fuel in a turbine between diffusion and premixed operations*. 1996, Google Patents.
8. Dean, A.J., *Combustor tuning*. 2001, Google Patents.
9. Gutmark, E., et al., *Suppression of combustion instability by geometrical design of the bluff-body stabilizer.* Journal of Propulsion and Power, 1995. **11**(3): p. 456-463.
10. James, D. *A solution for noise associated with a series staged DLE combustion system*. in *2002 4th International Pipeline Conference*. 2002. American Society of Mechanical Engineers.
11. Joshi, N.D., et al. *Development of a fuel air premixer for aero-derivative dry low emissions combustors*. in *ASME 1994 International Gas Turbine and Aeroengine Congress and Exposition*. 1994. American Society of Mechanical Engineers.
12. Krebs, W., et al., *Thermoacoustic design tools and passive control: Siemens power generation approaches.* Progress in Astronautics and Aeronautics, 2005. **210**: p. 89.
13. Linck, M., M. Armani, and A. Gupta. *Passive Control of Unstable Combustion in a Swirl-Stabilized Spray Combustor*. in *42nd AIAA Aerospace Sciences Meeting and Exhibit*. 2004. Reno.
14. Mick, W.J. and M.R. Cohen, *Method for staging fuel in a turbine in the premixed operating mode*. 1996, Google Patents.
15. Paschereit, C.O. and E. Gutmark, *Control of combustion instability and emissions by burner's exit geometry modifications.* AIAA Paper, 2004. **636**: p. 2004.
16. Polifke, W., J. Kopitz, and A. Serbanovic. *Impact of the fuel time lag distribution in elliptical premix nozzles on combustion stability*. in *7th AIAA/CEAS Aeroacoustics Conference*. 2001.
17. Scarinci, T. and J.L. Halpin. *Industrial trent combustor—combustion noise characteristics*. in *ASME 1999 International Gas Turbine and Aeroengine Congress and Exhibition*. 1999. American Society of Mechanical Engineers.

18. Scarinci, T., C. Freeman, and I. Day. *Passive control of combustion instability in a low emissions aeroderivative gas turbine*. in *ASME Turbo Expo 2004: Power for Land, Sea, and Air*. 2004. American Society of Mechanical Engineers.
19. Sims, G., R. Copplestone, and J. Tilston. *Performance Studies of Passive Damping Techniques Used to Suppress Combustion Oscillations in LPP Combustors*. in *ASME Turbo Expo 2003, collocated with the 2003 International Joint Power Generation Conference*. 2003. American Society of Mechanical Engineers.
20. Steele, R.C., et al. *Passive control of combustion instability in lean premixed combustors*. in *ASME 1999 International Gas Turbine and Aeroengine Congress and Exhibition*. 1999. American Society of Mechanical Engineers.
21. Tuthill, R.S., et al., *Swozzle based burner tube premixer including inlet air conditioner for low emissions combustion*. 2002, General Electric Company (Schenectady, NY).
22. McManus, K., T. Poinsot, and S. Candel, *A review of active control of combustion instabilities.* Progress in energy and combustion science, 1993. **19**(1): p. 1-29.
23. Blackstock, D.T., *Fundamentals of physical acoustics*. 2000: John Wiley & Sons.
24. Quinlan, J.M., Scarborough, D. E., Rehl, A., and Zinn, B. T., *NASA Final Report.* 2015.
25. Scarborough, D.E., *An Experimental and Theoretical Investigation of a Fuel System Tuner for the Suppression of Combustion Driven Oscillatioins.* Dissertation, 2010.
26. Knez, A.J., D.E. Scarborough, and B.T. Zinn, *Measuring and Modeling the Nonlinear Impedance of Area Discontinuities.* 2006.
27. Rayleigh, J.W.S.B., *The theory of sound*. Vol. 2. 1896: Macmillan.
28. Sivian, L., *Acoustic impedance of small orifices.* The Journal of the Acoustical Society of America, 1935. **7**(2): p. 94-101.
29. Ingard, U., *On the theory and design of acoustic resonators.* The Journal of the acoustical society of America, 1953. **25**(6): p. 1037-1061.
30. Ingård, U. and S. Labate, *Acoustic circulation effects and the nonlinear impedance of orifices.* The Journal of the Acoustical Society of America, 1950. **22**(2): p. 211-218.
31. Ingard, U. and H. Ising, *Acoustic nonlinearity of an orifice.* The journal of the Acoustical Society of America, 1967. **42**(1): p. 6-17.
32. Zinn, B.T., *A theoretical study of non-linear damping by Helmholtz resonators.* Journal of Sound and Vibration, 1970. **13**(3): p. 347-356.
33. Johnston, J. and W. Schmidt, *Measurement of acoustic reflection from an obstruction in a pipe with flow*. The Journal of the Acoustical Society of America, 1978. **63**(5): p. 1455-1460.
34. Cummings, A., *Acoustic nonlinearities and power losses at orifices.* AIAA journal, 1984. **22**(6): p. 786-792.
35. Morse, P.M. and K.U. Ingard, *Theoretical Acoustics*. 1968, New York: McGraw-Hill. 278-279.
36. Davidson, P.A., *Turbulence: an introduction for scientists and engineers*. 2015: Oxford University Press.
37. Scarborough, D.E., *An Experimental and Theoretical Investigation of a Fuel System Tuner for the Suppression of Combustion Driven Oscillations*, in *Mechanical Engineering*. 2010, Georgia Institute of Technology: Atlanta GA. p. 368.
38. Scarborough, D., A. Knez, and B. Zinn. *Measuring and Modeling the Nonlinear Acoustic Impedance of Area Discontinuities*. in *44th AIAA Aerospace Sciences Meeting and Exhibit*. 2006.

39. de Bree, H.-E., et al., *The μ-flown: a novel device for measuring acoustic flows.* Sensors and actuators A: Physical, 1996. **54**(1-3): p. 552-557.
40. De Bree, H.-E., et al. *The spl mu/-Flown-A Novel Device Measuring Acoustical Flows*. in *Solid-State Sensors and Actuators, 1995 and Eurosensors IX.. Transducers' 95. The 8th International Conference on*. 1995. IEEE.
41. de Bree, H., F. van der Eerden, and J. vAn HonscHotEn, *A novel technique for measuring the reflection coefficient of sound absorbing materials.* 2000.
42. Schurer, H., et al., *Comparison of two methods for measurement of horn input impedance.* Journal of the Audio Engineering Society, 1998. **46**(12): p. 1119-1125.
43. Fahy, F., *Rapid method for the measurement of sample acoustic impedance in a standing wave tube.* Journal of Sound and Vibration, 1984. **97**(1): p. 168-170.
44. Chung, J. and D. Blaser, *Transfer function method of measuring in-duct acoustic properties. I. Theory.* The Journal of the Acoustical Society of America, 1980. **68**(3): p. 907-913.
45. Chu, W.T., *Transfer function technique for impedance and absorption measurements in an impedance tube using a single microphone.* The Journal of the Acoustical Society of America, 1986. **80**(2): p. 555-560.
46. Chu, W., *Single-microphone method for certain applications of the sound intensity technique.* The Journal of the Acoustical Society of America, 1985. **78**(S1): p. S60-S60.
47. Chu, W., *Impedance tube measurements- a comparative study of current practices.* Noise control Engineering journal, 1991. **37**(1): p. 37-44.
48. Jones, M.G. and P.E. Stiede, *Comparison of methods for determining specific acoustic impedance.* The Journal of the Acoustical Society of America, 1997. **101**(5): p. 2694-2704.
49. Seybert, A.F. and D.F. Ross, *Experimental determination of acoustic properties using a two-microphone random-excitation technique.* the Journal of the Acoustical Society of America, 1977. **61**(5): p. 1362-1370.
50. Jang, S.-H. and J.-G. Ih, *On the multiple microphone method for measuring in-duct acoustic properties in the presence of mean flow.* The journal of the acoustical society of America, 1998. **103**(3): p. 1520-1526.
51. Katz, B.F., *Method to resolve microphone and sample location errors in the two-microphone duct measurement method.* The Journal of the Acoustical Society of America, 2000. **108**(5): p. 2231-2237.
52. ASTM, E., *1050–90, Standard Test Method for Impedance and Absorption of Acoustical Materials Using a Tube, Two microphones, and a Digital Frequency Analysis System Akshaya Jena and Krishna Gupta. 2002. Characterization of pore structure of filtration media.* Fluid/particle Separation Journal. **14**(3): p. 227-241.
53. Bodén, H. and M. Åbom, *Influence of errors on the two-microphone method for measuring acoustic properties in ducts.* The Journal of the Acoustical Society of America, 1986. **79**(2): p. 541-549.
54. Åbom, M. and H. Bodén, *Error analysis of two-microphone measurements in ducts with flow.* The journal of the acoustical society of America, 1988. **83**(6): p. 2429-2438.
55. Rice, E.J., *Theoretical study of the acoustic impedance of orifices in the presence of a steady grazing flow.* The Journal of the Acoustical Society of America, 1976. **59**(S1): p. S32-S32.

56. Ahuja, K., R. Gaeta Jr, and M. DAgostino, *High amplitude acoustic behavior of a slit-orifice backed by a cavity.* 2000.
57. Hersch, A. and B. Walker, *Effect of grazing flow on the acoustic impedance of Helmholtz resonators consisting of single and clustered orifices.* 1979.
58. Cummings, A., *The response of a resonator under a turbulent boundary layer to a high amplitude non-harmonic sound field.* Journal of Sound and Vibration, 1987. **115**(2): p. 321-328.
59. Howe, M., *The influence of grazing flow on the acoustic impedance of a cylindrical wall cavity.* Journal of Sound and Vibration, 1979. **67**(4): p. 533-544.
60. Jing, X., et al., *Effect of grazing flow on the acoustic impedance of an orifice.* AIAA journal, 2001. **39**(8): p. 1478-1484.
61. Malmary, C., et al. *Acoustic impedance measurement with grazing flow*. in *Proceedings of the 7th AIAA/CEAS Aeroacoustics Conference*. 2001.
62. Lee, S.-H. and J.-G. Ih, *Empirical model of the acoustic impedance of a circular orifice in grazing mean flow.* The Journal of the Acoustical Society of America, 2003. **114**(1): p. 98-113.
63. Jing, X. and X. Sun, *Sound-excited flow and acoustic nonlinearity at an orifice.* Physics of Fluids (1994-present), 2002. **14**(1): p. 268-276.
64. Ingård, U. and S. Labate, *Acoustic circulation effects and the nonlinear impedance of orifices.* The Journal of the Acoustical Society of America, 1950. **22**(2): p. 211-218.
65. Hersh, A.S. and T. Rogers, *Fluid mechanical model of the acoustic impedance of small orifices*. Vol. 2682. 1976: US National Aeronautics and Space Administration.
66. Bellucci, V., P. Flohr, and C.O. Paschereit, *Numerical and Experimental Study of Acoustic Damping Generated by Perforated Screens.* AIAA journal, 2004. **42**(8): p. 1543-1549.
67. Kirby, R. and A. Cummings, *The impedance of perforated plates subjected to grazing gas flow and backed by porous media.* Journal of Sound and Vibration, 1998. **217**(4): p. 619-636.
68. Dickey, N., A. Selamet, and M. Ciray, *An experimental study of the impedance of perforated plates with grazing flow.* The Journal of the Acoustical Society of America, 2001. **110**(5): p. 2360-2370.
69. Armstrong, D., *Acoustic grazing flow impedance using waveguide principles.* 1971.
70. Eldredge, J.D. and A.P. Dowling, *The absorption of axial acoustic waves by a perforated liner with bias flow.* Journal of Fluid Mechanics, 2003. **485**: p. 307-335.
71. EVERSMAN, W., et al., *Design of acoustic linings for ducts with flow.* Journal of Aircraft, 1972. **9**(8): p. 548-556.
72. A. Y. Gorenberg, E.N.L., M. A. Mironov, D. A. Perevalov, I. I. Sizov, *Selfinduced Sound Absorption by a Perforated Screen.* Russian Acoustical Society, 2001.
73. Sun, X., et al., *Effect of grazing–bias flow interaction on acoustic impedance of perforated plates.* Journal of Sound and Vibration, 2002. **254**(3): p. 557-573.
74. Meyer, E., F. Mechel, and G. Kurtze, *Experiments on the influence of flow on sound attenuation in absorbing ducts.* The Journal of the Acoustical Society of America, 1958. **30**(3): p. 165-174.
75. Bellucci, V., C.O. Paschereit, and P. Flohr, *Impedance of perforated screens with bias flow.* AIAA Paper, 2002. **2437**: p. 17-19.

76. Simonich, J., et al. *Development and qualification of an in-situ grazing flow impedance measurement facility*. in *12th AIAA/CEAS Aeroacoustics Conference, AIAA Paper 2006*. 2006.
77. Van Der Eerden, F., H. De Bree, and H. Tijdeman, *Experiments with a new acoustic particle velocity sensor in an impedance tube.* Sensors and Actuators A: Physical, 1998. **69**(2): p. 126-133.
78. Lambert, R. and E. Steinbrueck, *Acoustic synthesis of a flowduct area discontinuity.* The Journal of the Acoustical Society of America, 1980. **67**(1): p. 59-65.
79. Dupere, I. and A. Dowling, *The absorption of sound near abrupt axisymmetric area expansions.* Journal of sound and vibration, 2001. **239**(4): p. 709-730.
80. Gikadi, J., et al. *Linearized Navier-Stokes and Euler equations for the determination of the acoustic scattering behaviour of an area expansion*. in *18th AIAA/CEAS Conference*. 2012.
81. Munjal, M.L., *Acoustics of ducts and mufflers with application to exhaust and ventilation system design*. 1987: John Wiley & Sons.
82. Keefe, D.H., *Acoustical wave propagation in cylindrical ducts: Transmission line parameter approximations for isothermal and nonisothermal boundary conditions.* The Journal of the Acoustical Society of America, 1984. **75**(1): p. 58-62.
83. Rott, N., *Damped and thermally driven acoustic oscillations in wide and narrow tubes.* Zeitschrift für Angewandte Mathematik und Physik (ZAMP), 1969. **20**(2): p. 230-243.
84. Fahy, F.J., *Foundations of engineering acoustics*. 2000: Academic press.
85. Kinsler, L.E., et al., *Fundamentals of acoustics.* Fundamentals of Acoustics, 4th Edition, by Lawrence E. Kinsler, Austin R. Frey, Alan B. Coppens, James V. Sanders, pp. 560. ISBN 0-471-84789-5. Wiley-VCH, December 1999., 1999: p. 560.
86. Scarborough, D.E., *An Experimental and Theoretical Investigation of a Fuel System Tuner for the Suppression of Combustion Driven Oscillations*, in *Mechanical Engineering*. 2010, Georgia Institute of Technology: Atlanta GA. p. 368.